

# Miocene–Pleistocene deformation of the Saddle Mountains: Implications for seismic hazard in central Washington, USA

Lydia Staisch<sup>1,2,†</sup>, Harvey Kelsey<sup>3</sup>, Brian Sherrod<sup>2</sup>, Andreas Möller<sup>4</sup>, James Paces<sup>5</sup>, Richard Blakely<sup>1</sup>, and Richard Styron<sup>6,7</sup>

<sup>1</sup>Geology, Minerals, Energy, and Geophysics Science Center, U.S. Geological Survey, Menlo Park, California 94025, USA

<sup>2</sup>Earthquake Science Center, U.S. Geological Survey, University of Washington, Seattle, Washington 98195, USA

<sup>3</sup>Department of Geology, Humboldt State University, Arcata, California 95521, USA

<sup>4</sup>Department of Geology, University of Kansas, Lawrence, Kansas 66045, USA

<sup>5</sup>Geoscience and Environmental Change Science Center, U.S. Geological Survey, Denver, Colorado 80225, USA

<sup>6</sup>Earth Analysis, Seattle, Washington 98105, USA

<sup>7</sup>Global Earthquake Model Foundation, Pavia 27100, Italy

## ABSTRACT

The Yakima fold province, located in the backarc of the Cascadia subduction zone, is a region of active strain accumulation and deformation distributed across a series of fault-cored folds. The geodetic network in central Washington has been used to interpret large-scale N-S shortening and westward-increasing strain; however, geodetic data are unable to resolve shortening rates across individual structures in this low-strain-rate environment. Resolving fault geometries, slip rates, and timing of faulting in the Yakima fold province is critically important to seismic hazard assessment for nearby infrastructure and population centers.

The Saddle Mountains anticline is one of the most prominent Yakima folds. It is unique within the Yakima fold province in that the syntectonic strata of the Ringold Formation are preserved and provide a record of deformation and drainage reorganization. Here, we present new stratigraphic columns, U-Pb zircon tephra ages, U-series caliche ages, and geophysical modeling that constrain two line-balanced and retrodeformed cross sections. These new constraints indicate that the Saddle Mountains anticline has accommodated 1.0–1.3 km of N-S shortening since 10 Ma, that shortening increases westward along the anticline, and that the average slip rate has increased 6-fold since 6.8 Ma. Provenance analysis suggests that the source terrane for the Ringold Formation was similar to that of the modern Snake River Plain. Using new slip rates and structural constraints, we

calculate the strain accumulation time, interpretable as a recurrence interval, for earthquakes on the Saddle Mountains fault and find that large-magnitude earthquakes could rupture along the Saddle Mountains fault every 2–11 k.y.

## INTRODUCTION

The U.S. Pacific Northwest is a region of considerable seismic hazard, largely owing to the subduction of the Juan de Fuca, Gorda, and Explorer plates beneath North America and clockwise rotation of upper-crustal blocks (Fig. 1). Geodetic surveys show that modern strain accumulation extends far inboard of the Cascadia subduction zone (McCaffrey et al., 2007, 2013, 2016). Consequently, seismic hazards are not only concentrated near the plate boundary, but also in the backarc.

The Yakima fold province, located in central Washington State, is a region of active strain accumulation and distributed deformation across a series of roughly E-W-trending fault-cored anticlinal ridges (Fig. 1). The region undergoes approximately N-S shortening at  $2 \text{ mm yr}^{-1}$  due to convergence between the clockwise-rotating Oregon block to the south and the stable North American plate to the northeast (Wells et al., 1998; McCaffrey et al., 2000, 2013, 2016). Paleoseismic studies have highlighted past earthquake occurrence along several Yakima folds (Campbell and Bentley, 1981; West et al., 1996; Blakely et al., 2011). However, fault geometries, slip rates, and the general deformation history of the Yakima folds remain debated and are of critical importance to earthquake hazard assessment for nearby infrastructure, such as the Hanford Site, a large nuclear waste fa-

cility, and major dams along the Columbia and Yakima Rivers (Fig. 1; Geomatrix Consultants, 1996; Benjamin and Associates et al., 2012).

Seismicity, geodetic data, and gravity anomalies within the Yakima fold province share several patterns that may delineate important geologic features and boundaries. Within the region, earthquake epicenters tend to cluster near the Yakima Canyon and near the Saddle Mountains (Fig. 1). The Hog Ranch–Naneum anticline (Tabor et al., 1982) is located between these two seismically active regions and has been identified by high-resolution geodetic work as a potentially important boundary between two domains of strain within the Yakima fold province (McCaffrey et al., 2016). McCaffrey et al. (2016) also identified another boundary located immediately to the east of the Saddle Mountains (Fig. 1). These proposed strain boundaries correspond well with steep gradients in isostatic residual gravity anomaly data and are thus likely long-lived geologic features (Saltus, 1993; Blakely et al., 2011; Lamb et al., 2015). While geodetic data illuminate large-scale trends within central Washington, the overall strain rate is low, and noise within geodetic data obscures the signal of active deformation along individual fault-cored folds. The geologic record, on the other hand, encompasses enough time to clarify spatial and temporal variance in strain rate.

The Saddle Mountains anticline is the most prominent Yakima fold east of the Columbia River and is bracketed by the aforementioned boundaries in gravity and geodetic data (Fig. 1). Its topographic prominence in the landscape and proximity to infrastructure make it an ideal target for geologic investigation and hazard assessment. The majority of the Yakima fold province is composed of the Miocene Columbia River

†lstaisch@usgs.gov

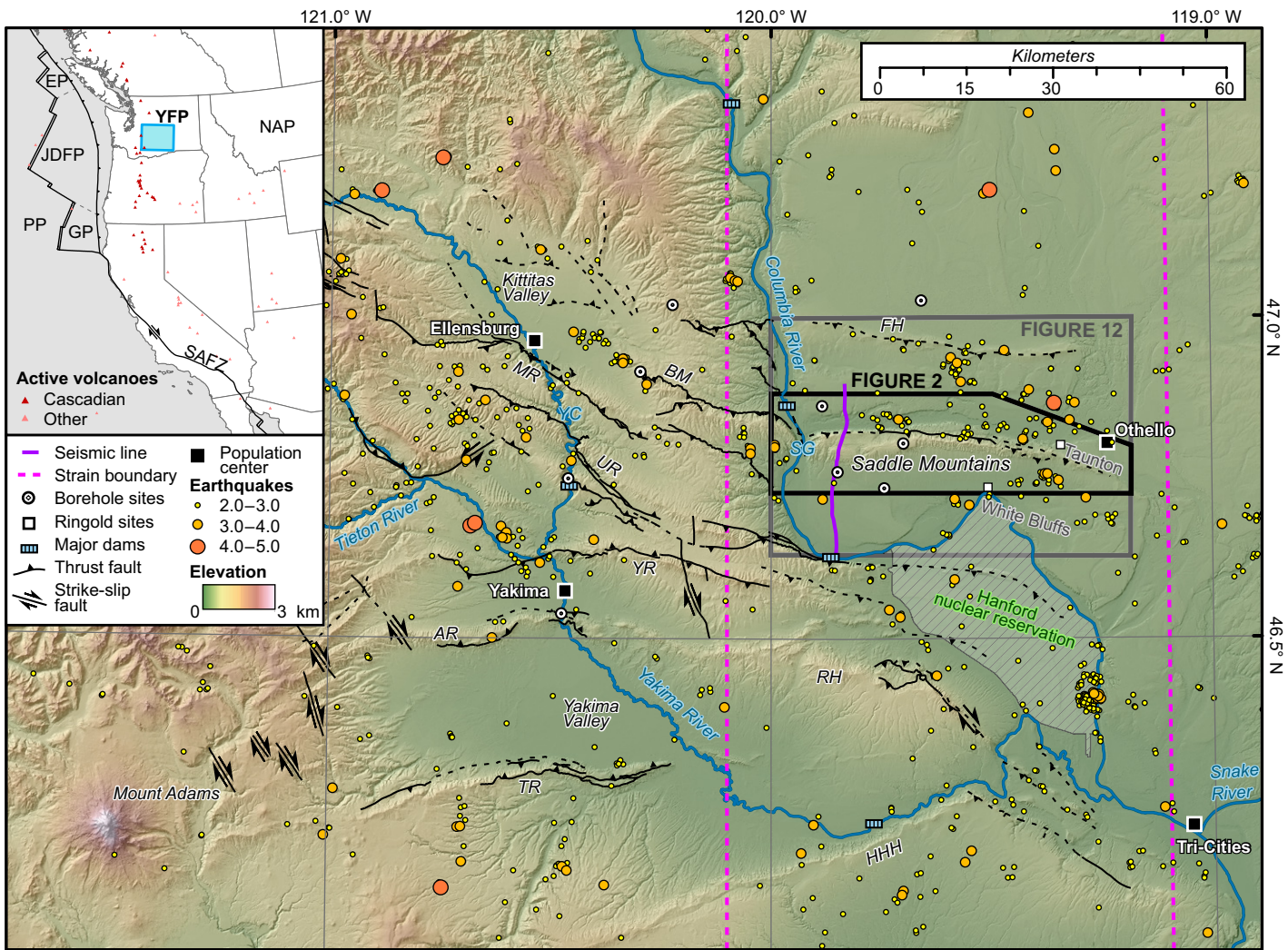


**Figure 1.** Regional map of the Yakima fold province, with inset showing the tectonic setting in the western United States for reference. Abbreviations on inset: PP—Pacific plate, NAP—North American plate, EP—Explorer plate, GP—Gorda plate, JDFP—Juan de Fuca plate, and SAFZ—San Andreas fault zone; YFP—Yakima fold province. Abbreviations on map: MR—Manastash Ridge, UR—Umtanum Ridge, YR—Yakima Ridge, AR—Ahtanum Ridge, TR—Toppenish Ridge, FH—Frenchman Hills, RH—Rattlesnake Hills, HHH—Horse Heaven Hills, BM—Boyleston Mountains, SG—Sentinel Gap, and YC—Yakima Canyon. Digital elevation model (DEM), and hillshade derivative, is from 10-m-resolution U.S. Geological Survey national map database ([ned.usgs.gov](http://ned.usgs.gov)). Active fault locations are from the U.S. Geological Survey Quaternary Fault database ([earthquake.usgs.gov/hazards/qfaults](http://earthquake.usgs.gov/hazards/qfaults)). Earthquake locations and magnitudes are from the Advanced National Seismic System (ANSS) earthquake catalog (<http://www.quake.geo.berkeley.edu/anss/catalog-search.html>). Borehole site locations are from Czajkowski et al. (2012). Strain boundary locations are from McCaffrey et al. (2016). The location of Figure 2 is indicated by a thick black outline.

Basalt Group, much of which has been stripped of less-consolidated suprabasaltic strata by catastrophic Pleistocene flooding. However, the Saddle Mountains anticline is unique among the Yakima folds in that the post–Columbia River Basalt Group Ringold Formation (Packer and Johnson, 1979; Repenning, 1987; Morgan and Morgan, 1995) is preserved in the hanging wall and footwall of the exposed Saddle Mountains fault (Reidel, 1988). The preservation of these terrestrial strata allows for expansion of the Saddle Mountains anticline deformation history into post–mid-Miocene time.

In this work, we examined the Ringold Formation and the magnitude of deformation of the Saddle Mountains anticline to reconstruct the chronology of deformation in central Washington. To establish the sedimentological response to deformation along the anticline, we measured the stratigraphy in the hanging wall and footwall of the Saddle Mountains fault, dated interbedded tephra using U-Pb zircon geochronology, dated variably deformed petrocalcic horizons using U-series geochronology, and determined the source of strata using U-Pb detrital zircon provenance analysis. We

evaluated spatial and temporal changes in the deformation rate along the Saddle Mountains anticline by measuring the offset along variably deformed marker beds. In addition, we constructed two new balanced cross sections, further constrained by modeling of high-resolution magnetic anomaly data, to document the magnitude of shortening and along-strike structural variability. Finally, we used these new constraints on the structure and deformation rates of the Saddle Mountains anticline to assess the seismic hazards posed to central Washington.

## GEOLOGIC BACKGROUND

The Saddle Mountains are a prominent structural feature of the Yakima fold province and form the northern boundary of the Pasco Basin in central Washington State. The Saddle Mountains are ~115 km long, spanning from the eastern edge of Kittitas Valley to just south of Othello, Washington (Fig. 1). The westward continuation of the Saddle Mountains, west of the Hog Ranch–Naneum anticline, is called the Boylston Mountains, which gradually bend to a NW–SE trend (Fig. 1).

### Stratigraphy

The Columbia River Basalt Group blanketed eastern Washington and Oregon in the Miocene (Reidel et al., 1989a, 1989b, 1994, 2013), and so the modern topography of the Yakima fold province has been generated since mid-Miocene time (Reidel, 1984; Watters, 1989). While the landscape of eastern and central Washington is largely mantled in Miocene flood basalts, exploratory oil and gas drilling has locally revealed the underlying stratigraphy. In the Saddle Mountains, boreholes BN 1–9 and AF 1–6 (Figs. 1 and 2; Czajkowski et al., 2012) reached depths >5.3 km and >4.3 km, respectively, and penetrated through the Columbia River Basalt Group and into the underlying Eocene and Oligocene strata (Fig. 3; Fig. DR1<sup>1</sup>). The 400–700 m of strata immediately beneath the Columbia River Basalt Group found in borehole logs have been assigned to the Ellensburg Formation (Czajkowski et al., 2012), which is typically a name given to undifferentiated clastic and volcanoclastic strata intercalated with and overlying the Columbia River Basalt Group (Bentley, 1977; Smith, 1988; Tolan et al., 2009; Cheney, 2014). Because of their stratigraphic position below the Columbia River Basalt Group, the units identified as Ellensburg Formation in boreholes BN 1–9 and AF 1–6 are more likely either the andesitic to basaltic Oligocene Fifes Peak or the clastic and tuffaceous Ohanapecosh Formations (Fig. 3; Fiske, 1963; Smith, 1988; Tabor et al., 2000; Cheney, 2014; Jutzeler et al., 2014). Logs from boreholes BN 1–9 and AF 1–6 indicate that basalt continues below the Columbia River Basalt Group strata (Wilson et al., 2008; Czajkowski et al., 2012), suggesting that the Oligocene strata are more likely the Fifes Peak Formation at these locations (Fig. DR1 [see footnote 1]). Beneath

the Oligocene strata, boreholes penetrate into 240–400 m of mid-Eocene Wenatchee Formation and 520–1420 m of mid-late Eocene Roslyn Formation, both of which are typically fluvial and lacustrine in lithology (Fig. 3; Fig. DR1 [see footnote 1]; Tabor et al., 1984; Miller et al., 2009; Gilmour, 2012; Cheney, 2014). Neither borehole AF 1–6 nor BN 1–9 penetrates into basement rock. North of the Saddle Mountains, boreholes Brown 7–24 and Quincy No. 1 penetrate into underlying Oligocene and Eocene strata, and the latter terminate in basement rock, thus limiting the pre-Miocene stratigraphic thickness locally to 1690 m (Fig. DR1 [see footnote 1]). Overall, the boreholes drilled near the Saddle Mountains show a northward thinning of pre-Miocene strata.

The oldest rock unit exposed on the Saddle Mountains is the Grande Ronde Basalt, part of the Columbia River Basalt Group, emplaced 16.0–15.6 Ma (Fig. 3; Swanson et al., 1979; Camp, 1981; Barry et al., 2013). The Grande Ronde Basalt is divided into four major sections based on geomagnetic polarity. From oldest to youngest, these sections are R<sub>1</sub>, N<sub>1</sub>, R<sub>2</sub>, and N<sub>2</sub>, and each section is further divided into individual flow groups based on geochemistry (Reidel, 1983; Reidel et al., 2013). The majority of Grande Ronde Basalt exposures in the Saddle Mountains are of the upper, normal-polarity N<sub>2</sub> flows, which include the Sentinel Bluffs Member (Tsb; Fig. 2). However, exposures of the underlying, reverse-polarity R<sub>2</sub> flows are observed near Sentinel Gap, including the Schwana geochemical group (Ts; Fig. 2; Coe et al., 1978; Reidel, 1984).

The Wanapum Basalt stratigraphically overlies the Grande Ronde Basalt (Fig. 3). In the Saddle Mountains, exposures of this unit are limited to the Frenchman Springs (Tf), Roza (Tr), and Priest Rapids Members (Tpr), which were emplaced ca. 15.5–14.5 Ma (Swanson et al., 1979; Camp, 1981; Reidel and Fecht, 1981). Within the Pasco Basin, south of the Saddle Mountains, other Wanapum Basalt flows have been mapped, but they are less laterally extensive and did not reach the Saddle Mountains (Reidel and Fecht, 1981).

The Saddle Mountains Basalt overlies the Wanapum Basalt (Fig. 3). The Huntzinger Flow (Th; 13.3–13.0 Ma), Pomona (Tp; 12.0–10.9 Ma), Elephant Mountain (Tem; 10.5–10.0 Ma), and Ice Harbor (8.8–8.5 Ma) Members of the Saddle Mountains Basalt are exposed in the Saddle Mountains and were erupted between ca. 14 and 8.5 Ma (Swanson et al., 1979; Camp, 1981; Reidel and Fecht, 1981, 1987; Reidel et al., 2013). The Ice Harbor Member exposures are very limited on Saddle Mountain (Reidel, 1988), and thus the majority of the

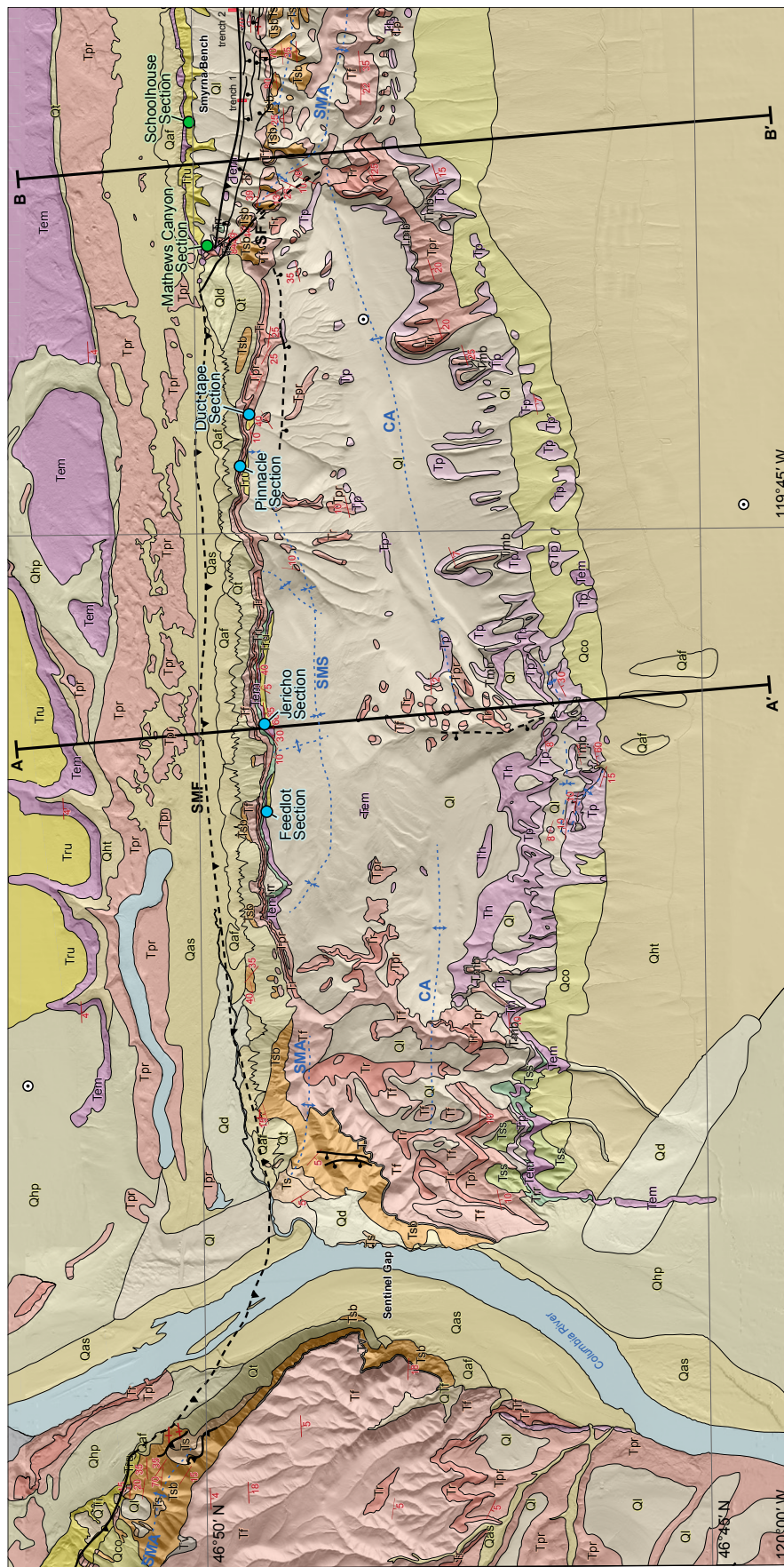
Columbia River Basalt Group strata along the Saddle Mountains were erupted prior to 10 Ma.

The majority of suprabasaltic strata in the Saddle Mountains are exposed on Smyrna Bench, in the footwall of the Saddle Mountains fault (Tr; Figs. 2 and 3). However, limited outcrops of strata have been identified on the hanging wall of the Saddle Mountains fault (Fig. 2; Reidel, 1988). The age of suprabasaltic strata in the footwall and hanging wall of the Saddle Mountains fault was not geochronologically or biostratigraphically constrained prior to this work. Existing mapping shows that these units overlie the 10.5–10.0 Ma Elephant Mountain Member and have been interpreted to be part of the Miocene–Pliocene Ringold Formation (Packer and Johnson, 1979; Repenning, 1987; Reidel, 1988; Morgan and Morgan, 1995). Paleomagnetic studies conducted on the Taunton and White Bluffs exposures concluded that deposition of the upper Ringold Formation occurred during the Gilbert Epoch (Packer and Johnson, 1979) identified by Gradstein et al. (2012) as 6.033–3.596 Ma. Mammalian and fish fossil evidence suggests that deposition continued into the Kaena subchron of the Gauss Epoch (Morgan and Morgan, 1995; Repenning, 1987), from 3.032 to 3.116 Ma (Gradstein et al., 2012). However, the outcrops on the Saddle Mountains differ from typical Ringold Formation strata, which is best exposed at the White Bluffs along the Columbia River and near the town of Taunton, Washington, southeast of the Saddle Mountains, respectively (Fig. 1). Specifically, outcrops along the Saddle Mountains include a much greater volume of conglomeratic strata, compared to the strata dominated by lacustrine and paleosols facies along the White Bluffs and near Taunton. Furthermore, lithofacies and stratigraphic thicknesses of the Ringold Formation vary significantly and may record local geologic events, such as deformation along a nearby structure, as well as large-scale events, such as drainage reorganization (Lindsey and Gaylord, 1990).

### Structure

The dominant structure of the Saddle Mountains is the E–W–trending, N–vergent, asymmetrical Saddle Mountains anticline, which is cored by the S-dipping Saddle Mountains reverse fault. The Crest anticline and the Smyrna monocline are smaller structures on the Saddle Mountains that similarly trend E–W (Figs. 1 and 2). Other structural features of the Saddle Mountains include the less apparent NW–SE–trending Smyrna fault and a small but well-exposed anticline located near the western extent of the Crest anticline (Fig. 2).

<sup>1</sup>GSA Data Repository item 2017325, Figures DR1–DR4, and Tables DR1–DR11, is available at <http://www.geosociety.org/datarerepository/2017> or by request to editing@geosociety.org.



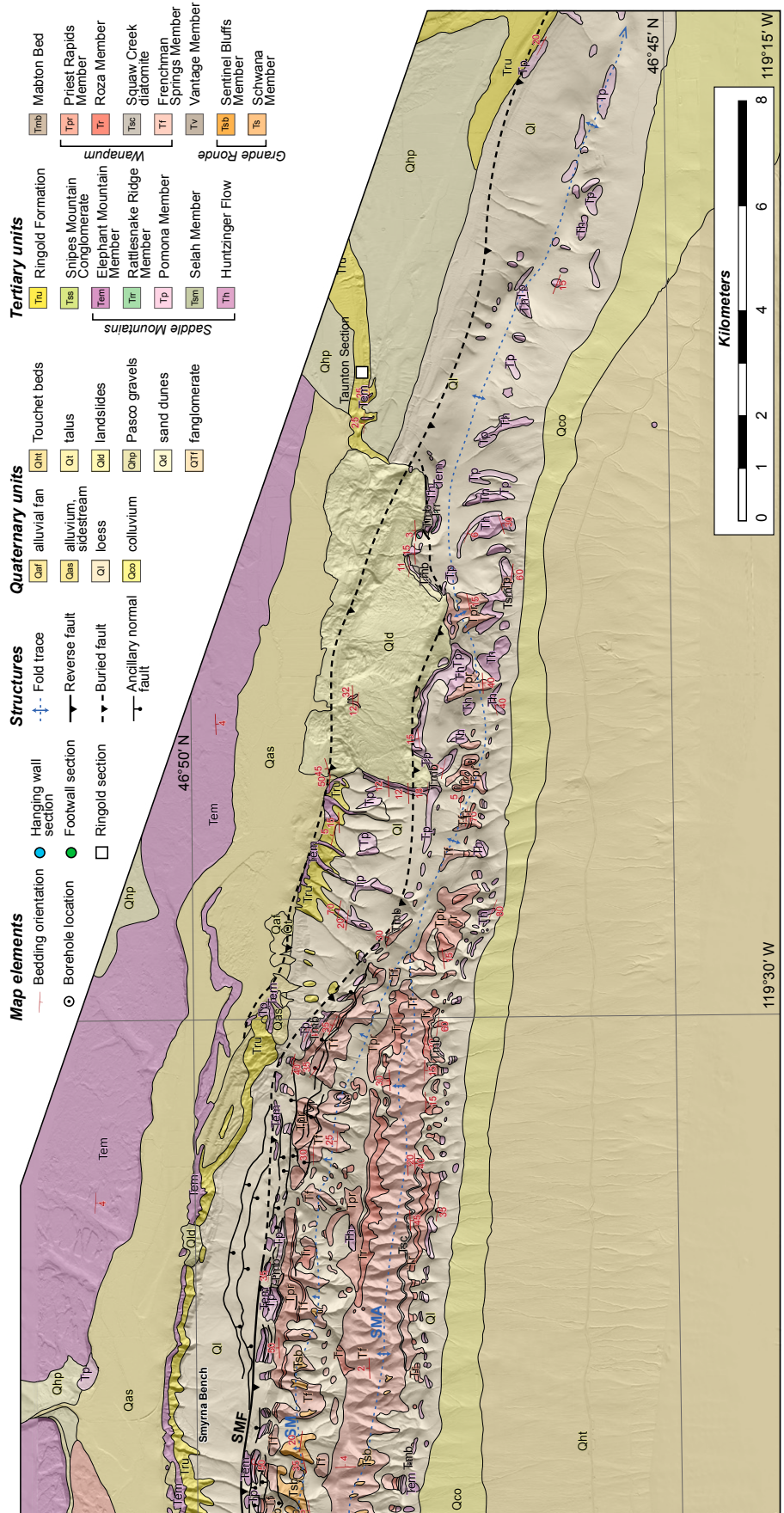
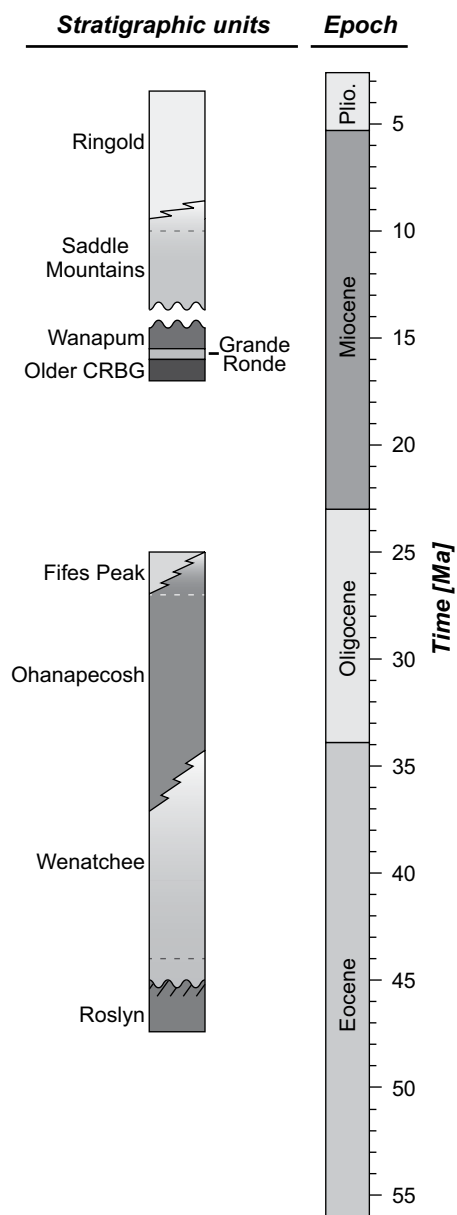


Figure 2 (*continued*).

**Figure 3. Generalized stratigraphy of the Saddle Mountains, based on exploratory borehole measurements (Fig. DR1 [see footnote 1]) and previous work on the relative ages of geologic units in the Cascadian backarc (Fiske, 1963; Bentley, 1977; Packer and Johnson, 1979; Swanson et al., 1979; Camp, 1981; Reidel and Fecht, 1981, 1987; Tabor et al., 1984; Repenning, 1987; Reidel, 1988; Smith, 1988; Morgan and Morgan, 1995; Tabor et al., 2000; Miller et al., 2009; Tolan et al., 2009; Gilmour, 2012; Barry et al., 2013; Reidel et al., 2013; Cheney, 2014; Jutzeler et al., 2014; this work]). Faded regions indicate time periods during which the depositional age of a unit is disputed, with dashed lines as alternative depositional cessation. “Shazam” lines indicate possible coeval deposition of temporally overlapping units. CRBG—Columbia River Basalt Group; Plio.—Pliocene.**



During the latest Pleistocene, several catastrophic outburst floods from glacial Lake Missoula flowed through the Crab Creek scablands-channel system, along the northern margin of the Saddle Mountains, and incised through the Saddle Mountains at what is now Sentinel Gap (Smith, 1993). The floods through the Crab Creek channel likely eroded the western extent of the Smyrna Bench (Fig. 2) and bared a cross-sectional exposure of the Saddle Mountains fault (Fig. 4). At the exposure of the Saddle Mountains fault and along Smyrna Bench, the Saddle Mountains fault places Miocene Columbia River Basalt Group in the hanging wall over the Smyrna Bench, which is composed of Columbia River Basalt Group strata and suprabasaltic strata. Further west, the Saddle Mountains fault footwall is not well exposed due to glacial outburst flood erosion and concealment beneath alluvial fans. East of the Smyrna Bench, the Saddle Mountains fault does not appear to be exposed, as the Elephant Mountain Member is folded at the surface, but not faulted (Fig. 2; Reidel, 1988).

Based on seismic-reflection data collected near Sentinel Gap, Casale and Pratt (2015) argued for two possibilities for Saddle Mountains fault geometry at depth: (1) a low-angle fault geometry, which would require a two stacked décollements at depth, or (2) a high-angle fault geometry, which would require the Saddle Mountains fault trace to be several hundreds of meters north of its current mapped location. We note that alluvium obscures the fault location along the seismic-reflection transect (Fig. 2). The two proposed models vary not only in fault geometry at depth, but also in the potential

earthquake hazards posed to central Washington. Casale and Pratt (2015) argued that the high-angle fault geometry model increases the area over which a single earthquake along the Saddle Mountains fault could rupture, and thus increases the maximum magnitude of potential seismic events to  $M > 7.5$ .

Structural and geophysical observations suggest that there may be a component of lateral shear accommodated near the Saddle Mountains. High-resolution aeromagnetic data show strong magnetic anomalies along the Smyrna anticline, which may relate to ponding of basalts along the eastern edge of the anticline (Reidel, 1984; Blakely et al., 2011). The Smyrna fault, which is parallel to and west of the Smyrna anticline, accommodates minor right-lateral offset based on

displacement of Columbia River Basalt Group flows (Reidel, 1984). Similarly, Reidel (1984) suggested that the Saddle Mountains anticline is offset by 2.7 km on either side of the Sentinel Gap (Fig. 2). Alternatively, offset may be accommodated by bending of the anticlinal crest or by lateral or oblique ramps along the Saddle Mountains fault. Evidence for either model is obscured by erosion along the Columbia River.

#### Previous Work on the Timing of Deformation

While deformation along the Saddle Mountains is mainly preserved in the Columbia River Basalt Group, several studies have suggested that deformation initiated prior to the Miocene and continues today (Malone et al., 1975; West et al., 1996; Casale and Pratt, 2015). Seismic-reflection data across the Saddle Mountains reveal a steepening of bedding orientations below ~4 km depth (Pratt, 2012; Casale and Pratt, 2015). Results from borehole BN 1–9, drilled at the hinge of the Crest anticline (Czajkowski et al., 2012), indicate that the change in bedding orientations may occur between the Eocene Roslyn Formation (48–45 Ma; Tabor et al., 1984; Miller et al., 2009; Cheney, 2014) and the overlying mid-Eocene Wenatchee Formation (>44.5–34[?] Ma; Tabor et al., 1984; Gilmour, 2012; Cheney, 2014). This may suggest that displacement was accommodated along the Saddle Mountains anticline and/or Saddle Mountains fault between mid-late Eocene and early Oligocene time. Seismic-reflection and borehole data do not penetrate beneath the Roslyn Formation, and so we have little insight as to whether the initiation of deformation along the Saddle Mountains anticline and Saddle Mountains fault preceded or postdated Eocene deposition.

Variations in basalt flow thickness have been used to constrain the timing of deformation (Reidel, 1984). Thinning of the Grande Ronde Basalt toward the E-W-trending anticlinal ridges near Sentinel Gap and near the Smyrna anticlinal ridge may suggest that deformation on the Saddle Mountains fault–Saddle Mountains anticline system was active during deposition from 16.0 to 15.6 Ma (Reidel, 1984). Similarly, the Huntzinger and Pomona flows (13.3–10.9 Ma) thin northward and do not extend north of the Saddle Mountains anticline, which may also relate to syndepositional deformation (Reidel, 1984). However, the more recent borehole data show continued thinning of Columbia River Basalt Group units north of the Saddle Mountains anticline (Fig. DR1 [see footnote 1]), suggesting that this variation in flow thickness could alternatively have been controlled by subsidence of the Pasco Basin (Reidel et al., 1989a, 2013),

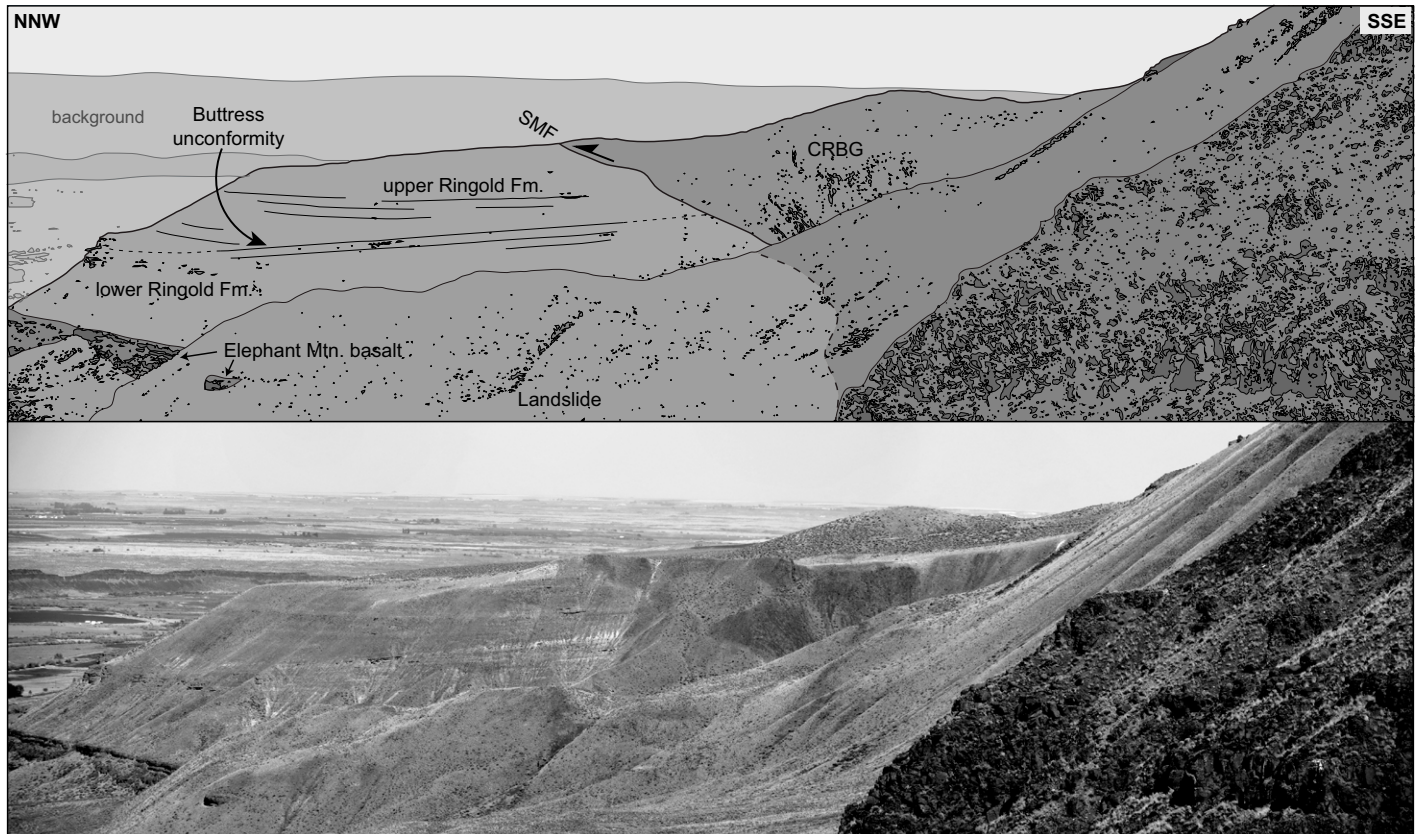


**Figure 4.** Photograph and photo interpretation of an exposure of the Saddle Mountains fault (SMF) near the Mathews Canyon section. The lower Ringold strata exhibit beds inclined to the south, whereas the upper lacustrine Ringold strata are subhorizontal. Here, the Saddle Mountains fault places Grande Ronde N2 Columbia River Basalt Group (CRBG) strata, locally overturned, on top of the Ringold Formation. The Ringold Formation measured 120 vertical meters in this photo. Photo by L. Staisch.

rather than being controlled by local anticlinal growth. We note that these two hypotheses are not mutually exclusive.

Folding of the Ringold Formation in the hanging wall of the Saddle Mountains fault suggests that N-S shortening across the Saddle Mountains fault likely continued into late Miocene–Pliocene time (Reidel, 1984). A paleoseismic study conducted along the Smyrna Bench provided evidence for Holocene deformation along the Saddle Mountains fault (West et al., 1996). Additionally, composite stress tensors from microearthquakes near the Saddle Mountains are compatible with N-S shortening and thus may indicate modern activity along the Saddle Mountains fault and associated anticlines (Malone et al., 1975).

## STRATIGRAPHY

In this work, we present six new stratigraphic sections measured in the suprabasaltic Ringold Formation near the Saddle Mountains. Four stratigraphic sections were measured in the hanging wall of the Saddle Mountains fault,

and two sections were measured in the footwall (Figs. 2 and 5). Sections were measured at decimeter scale, and the base of all sections began at the top of the 10–10.5 Ma Elephant Mountain Member of the Saddle Mountains Basalt (Reidel, 1984). Strata measured in the hanging wall of the Saddle Mountains fault were typically very well exposed (Fig. 6A). The quality of exposure of footwall strata was more variable, ranging from excellent to moderate.

We identified 11 distinct lithofacies in the hanging wall and footwall strata of the Saddle Mountains (Table 1). Facies V1 and V2 represent volcanic units interbedded within the Ringold Formation. Given its stratigraphic position above the Elephant Mountain Member, the weathered basalt (facies V1) is likely one of the smaller Saddle Mountain Basalt flows erupted during the waning stages of Columbia River Basalt Group volcanism (Reidel, 1984; Reidel et al., 2013). Facies V2 is interpreted as air-fall tuff erupted during sediment accumulation along the Saddle Mountains anticline. Facies C1–C4 are dominantly conglomeratic or associated with conglomerate strata (Table 1).

Facies L1 and L2 are associated with lacustrine strata, which are only present in the upper footwall sections. These facies are similar to those documented in most other studies of the Ringold Formation (Packer and Johnson, 1979; Repenning, 1987; Lindsey and Gaylord, 1990; Morgan and Morgan, 1995; Lindsey, 1996). Facies A1 represents eolian loess and is found throughout the measured strata. Facies P1 and P2, found throughout the measured strata, are pedogenic horizons that represent soil formation during depositional hiatuses. Soil structure varies from weak blocky to well-developed prismatic, suggesting variable durations of land surface stability. Vertical burrows and root casts are common in paleosols. Petrocalcite horizons (i.e., caliche) developed within layers of open-framework conglomeratic, eolian, and lacustrine strata (Figs. 6B, 6C, 6E, and 6F) and typically developed within and above root-bearing strata (Fig. 6D). Calcified horizons exhibit a range of development stages, from early stages with thin calcic layers (Fig. 6C) to late stages with complete and dense calcification of the strata (Figs. 6B and 6E).

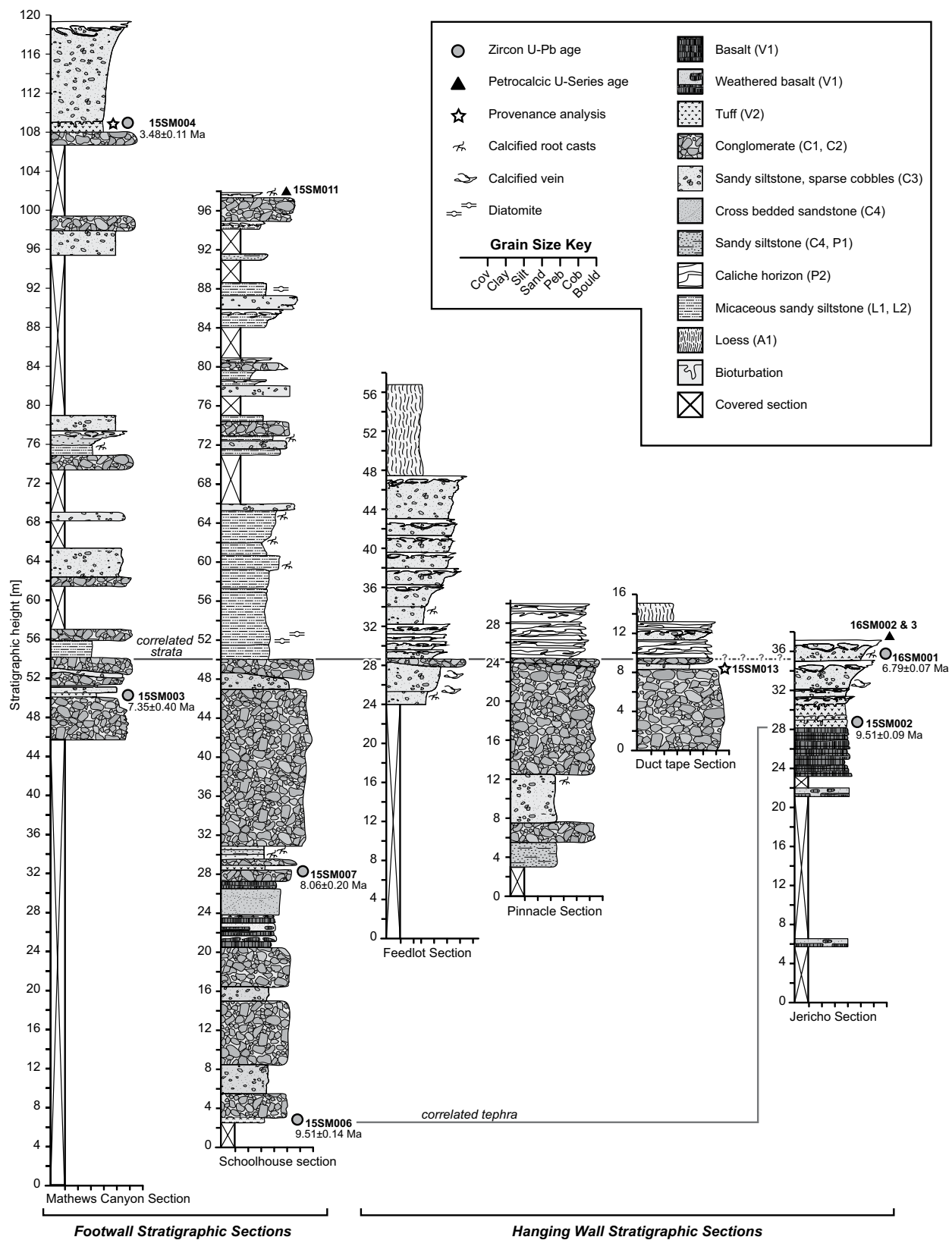


**Figure 5.** Stratigraphic columns measured in the Ringold Formation near the Saddle Mountains. Stratigraphic sections are organized from west (left) to east (right) and are hung on the common marker bed horizon identified in five out of six sections. The base of each stratigraphic column is on the top of the Elephant Mountain Member (meter 0). Samples collected from strata are located to the right of each stratigraphic column and are identified by sample type (symbol) and ID number. Cov—covered, Peb—pebble, Cob—cobble, Bould—boulder.

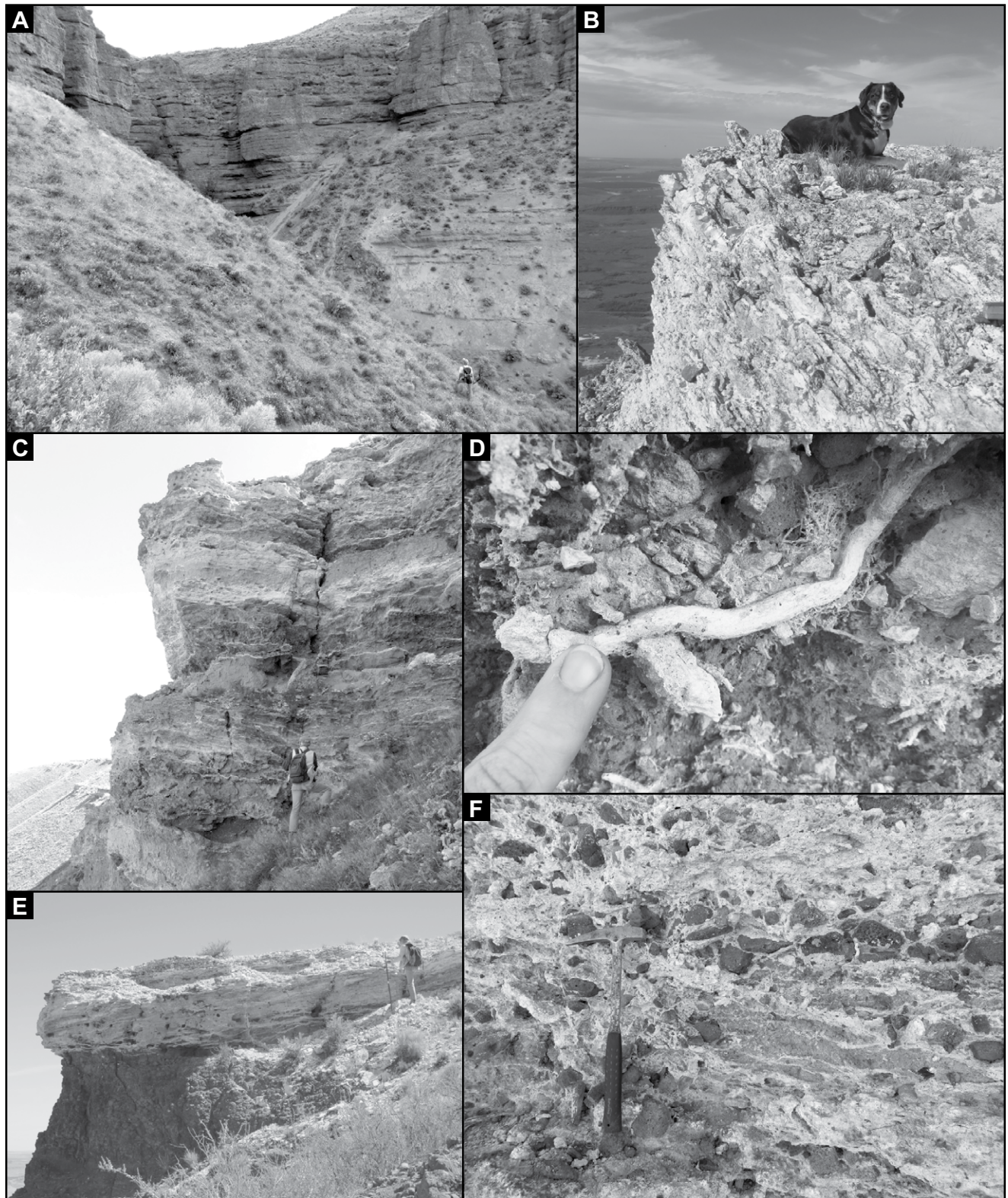


**Figure 6.** Field photos of the Ringold Formation near the Saddle Mountains anticline. (A) Photo of footwall conglomeratic section with Harvey Kelsey for scale, taken near the Schoolhouse section (Fig. 5). (B) Steeply dipping petrocalcic horizon near the Jericho section (Fig. 5) with Jura Staisch for scale. (C) Photo of hanging-wall debris flow and paleosols horizons with Harvey Kelsey for scale, taken near Feedlot section (Fig. 5). (D) Calcified rhizoliths from paleosol horizon in Schoolhouse section. (E) Petrocalcite horizon developed directly on Elephant Mountain Member, with Harvey Kelsey for scale. (F) Calcic cement developed in mudflow strata of the Jericho section, with rock hammer for scale. Photos by L. Staisch.

TABLE 1. STRATIGRAPHIC LITHOFACIES DESCRIPTIONS AND INTERPRETATIONS

Facies	Facies description	Facies interpretation
V1	Weathered, thinly layered basalt flows. Basalt is dark gray and iridescent, occasionally orange to red when oxidized.	Basaltic eruption during the waning stages of Saddle Mountains Basalt volcanism.
V2	Reddish beige tephra layers with 1–2-mm-sized lapilli and occasionally with 2–3-mm-sized light-colored pumice clasts. Layers are 0.3–0.8 m thick and are occasionally strongly bioturbated in the upper 0.1–0.2 m of the deposit.	Air-fall tuff eruption coincident with deposition. Some layers may be fluvially or biologically reworked.
C1	Open-closed framework conglomerate with subangular to subrounded basaltic clasts. Clasts are poorly sorted, and imbrication is crude or absent. Clast size is pebble to boulder, with modal size of pebble-cobble. Clasts are entirely composed of basalt and make up 70%–85% of the deposits. The matrix is composed of medium to coarse sandstone. Conglomerate beds are 0.2–4.0 m thick and have nonerosive bases.	Debris-flow deposit. Clast angularity and poor sorting suggest little to no fluvial transport. Clast lithology suggests that the majority of material was locally sourced from the emergent Saddle Mountains anticline.
C2	Moderate- to well-sorted closed-framework conglomerate with strongly imbricated basaltic clasts. Erosive bases occasionally scour deeply inset into prior deposits. Deposits are 0.5–1.0 m thick. Clasts are pebble to cobble in size and are subrounded to rounded. Clast lithology is entirely basaltic.	Fluvial channel-fill deposits. Scoured base and imbrication suggest that these layers were deposited in an energetic fluvial setting. Lack of boulder-sized clasts limited the maximum competence of the fluvial setting.
C3	Beige to gray silty sandstone, typically structureless with sparse floating pebbles (10%–15%). Sandstone layers range from medium to coarse in grain size and range between 0.5 and 2.0 m in thickness. Sand lithology is dominantly basaltic. Clasts are also basaltic and subrounded.	Sandy mudflows. Typically interbedded with coarser debris-flow deposits (C1).
C4	Beige to tan sandy siltstone and interbedded sandstone. Laminated and rarely cross-bedded. Sandstone layers range from fine to coarse in grain size and range between 0.2 and 0.8 m in thickness. Sand lithology is dominantly basaltic. Some layers are heavily bioturbated. Found in association with C2.	Overbank deposits accumulated on bar flanks. Cross-bedding and lack of conglomeratic strata are suggestive of a less energetic fluvial depositional setting than facies C2.
L1	Light-gray to white siltstone with occasional interbedded diatomite layers. Layers are finely and subhorizontally laminated. Siltstone and sandstone layers show occasional cross-bedding but typically do not show strong evidence of fluvial transport. Some layers show evidence of pedogenesis, such as root casts.	Epilimnetic lake setting. Found in association with facies L2, P1, and P2 and thus likely suggests that lakes were balanced-fill shallow-water bodies. This facies is found only in the footwall strata.
L2	Beige to light-brown silty fine sandstone with rare cross-bedded layers. Typically finely laminated and between 0.2 and 0.4 m in thickness. Notable difference from facies C4 is the presence of mica and quartz sand. Some layers are heavily bioturbated.	Suspended sediment carried into lacustrine setting via streams. The shift in sand lithology likely represents either a change in sediment source or addition in sediment source, compared to facies C4.
A1	Silt grain size and no internal structure. Found interbedded with closed-framework conglomerate and capping several sections. The upper portion of some silt layers contains natural soil aggregates and grades into facies P1.	Eolian loess deposit. When interbedded with other strata, these layers represent a hiatus in deposition.
P1	Light-brown to medium-brown siltstone and fine sandstone with granular or medium prismatic soil structure. Often containing root casts and/or evidence for strong bioturbation. Pedogenic structure often grades downward into parent siltstone or sandstone.	Soil formation and depositional hiatus. Paleosols within conglomeratic strata represent a temporarily abandoned alluvial-fan setting. Paleosols are relatively common in lacustrine strata, suggesting frequent drying of lake systems.
P2	White to light-beige calcified horizons are developed within some loess layers (A1), sandstone layers (C3–4 and L2), lacustrine siltstone (L1), and conglomerate (C1). Calcification ranges in development from thin layers (<0.1 m thick) to complete calcification of original strata (>2 m thick).	Soil formation and desiccation. Calcification of strata likely represents later stages of pedogenesis in an arid environment.

## Footwall Strata

Measured footwall stratigraphic sections include the Schoolhouse section (SH) in the east and the Mathews Canyon section (MC) in the west (Figs. 2 and 5). Footwall strata exhibit all depositional facies listed in Table 1. The base of the footwall section is well exposed in SH and is dominated by debris flows (facies C1) and mudflows (facies C3) with interbedded thin weathered basalt and tephra (facies V1 and V2, respectively; Figs. 5 and 6A). The lower ~50 m section of SH and MC is capped by an ~1-m-thick strongly imbricated conglomeratic layer with a well-defined basal scour (facies C2; Fig. 5). Above this layer, the strata change abruptly to lacustrine siltstone-dominated strata (L1–L2) that were deposited in a buttress unconformity with the coarser strata below (Fig. 4). The boundary between dominantly colluvial to dominantly lacustrine depositional facies occurs at ~290 m elevation, which correlates well with the base of the Taunton Ringold section, located

to the east (Fig. 7; Packer and Johnson, 1979). Based on interbedded L1 and L2 facies strata, we infer a balance-filled lake system wherein fluctuating lake level was common (Olsen, 1990; Carroll and Bohacs, 1999). Because thin conglomeratic layers (facies C2 and C4) interbedded within the lacustrine strata are more common toward the top of the measured strata (Fig. 5), we infer that the lacustrine system became progressively more overfilled with minimal lake fluctuation (Olsen, 1990; Carroll and Bohacs, 1999). The tops of finer layers (facies C2, C4, L1, L2, A1) occasionally show granular structure, root casts, and petrocalcification, which are indicative of periods of landscape stability.

From the footwall strata, we collected several samples for U-Pb zircon and U-series age analyses, and for U-Pb zircon provenance analysis. In stratigraphic order, tephra samples for stratigraphic age control are 15SM006, collected at the base of SH, 15SM007, collected within the dominantly conglomeratic section of SH, and 15SM003, collected near the top of

the dominantly conglomeratic section of MC (Fig. 5). We also analyzed one reworked tephra in MC for U-Pb zircon provenance analysis (15SM004). Sample 15SM011 is a collection of calcified root casts sampled at the top of SH for U-series dating.

## Hanging-Wall Strata

From east to west, the four stratigraphic sections measured in the hanging wall of the Saddle Mountains fault include the Duct tape (DT), Pinnacle (PN), Jericho (JR), and Feedlot (FL) sections (Figs. 2 and 5). These locations were chosen for stratigraphic analysis based on quality of exposure and available age control. Facies L1 and L2 are absent from the hanging-wall strata, but all others are present (Table 1). Facies V1 is only present in JR and is capped by a 1.2-m-thick lapilli tuff. For facies C1 and C3 in the hanging-wall strata, conglomerate is more prevalent in the eastern two stratigraphic sections (DT, PN), which is likely because DT

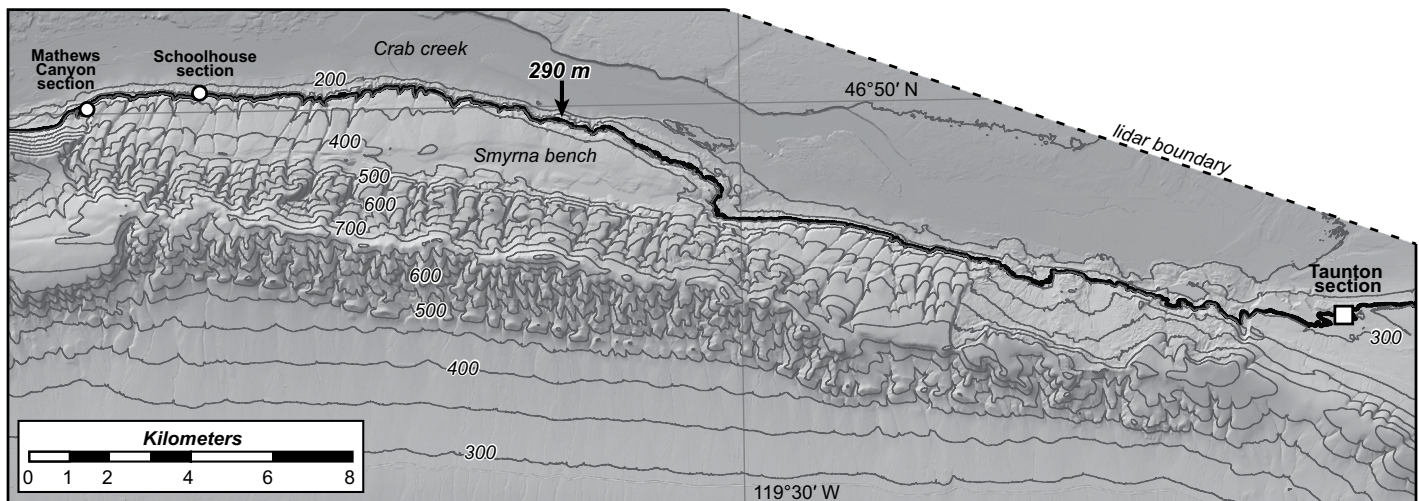


**Figure 7.** Topographic map of the eastern portion of the Saddle Mountains anticline with a 50 m contour interval (lidar—light detection and ranging). The base of the upper Ringold strata, at elevation 290, is identified by a thick black line. This correlates to the elevation of the Taunton Ringold section, which was magnetostratigraphically dated by Packer and Johnson (1979) at 6.033–3.596 Ma.

and PN sections are situated along the north slope of the Saddle Mountains anticline in a region that would accommodate more detritus from hillslope erosion compared to the JR and FL sections (Fig. 2). Conglomeratic strata commonly fine upward into loess-rich deposits with petrocalcic horizons (Fig. 5).

A distinctive conglomerate layer was the basis for a key correlation of hanging-wall and footwall strata and in turn allowed us to calculate vertical separation across the Saddle Mountains fault. Facies C2 is present as the uppermost conglomeratic layer in hanging-wall sections DT and PN and is the only closed-framework conglomeratic layer in hanging-wall section FL. It is absent from section JR (Fig. 5). Because facies C2 is also present as a single layer in the footwall sections SH and MC, we infer that the distinctive facies C2 in the hanging-wall and footwall strata are correlated horizons that were originally deposited at the same elevation (Fig. 5).

Within the hanging-wall facies, we sampled two tephra layers from the JR section (15SM002, 16SM001). The lowermost sample was taken from directly above the weathered basalt, and the uppermost was taken near the top of the JR section, directly below the capping caliche horizon (Fig. 5). One sample was taken for U-Pb zircon provenance analysis, collected from a reworked tephra layer in DT (15SM013; Fig. 5). The overlying caliche horizon is locally steeply dipping (Fig. 6B) within a hanging-wall fold (Fig. 8), suggesting deformation continued after calcification of the petrocalcic horizon. We sampled the deformed caliche layer for U-series age analysis (16SM002, 16SM003; Fig. 5).

## GEOCHRONOLOGY

### U-Pb Zircon Geochronology

We analyzed seven samples for U-Pb zircon analysis via laser ablation–inductively coupled plasma–mass spectrometry (LA-ICP-MS). Five tephra samples were analyzed for age of volcanic eruption (15SM002, 15SM003, 15SM006, 15SM007, 16SM001), one sandstone sample was analyzed for detrital zircon ages (15SM013), and one reworked tephra sample was analyzed for both detrital zircon and volcanic eruption ages (15SM004; Fig. 5). A detailed explanation methodology of U-Pb zircon age analysis is available in the Appendix.

For tephra samples, between 55 and 139 individual zircon crystals were analyzed, depending on the quality of the sample. Geological ages were determined using the maximum number of spot analyses able to define the youngest coherent age group with  $n \geq 3$ . This follows an approach discussed by Dickinson and Gehrels (2009) to reliably determine the maximum depositional ages of strata. Because the samples investigated here are mostly volcaniclastic, the ages of the youngest major zircon populations are interpreted to be more reliable than age groups with very low  $N$ , single youngest grains, or two grains. Those youngest grains were treated as outliers and possible contamination by strata from higher levels, which is difficult to avoid in semiconsolidated volcaniclastic material.

For provenance samples, at least 100 crystals were analyzed for each sample. Detrital zircon age spectra from the Saddle Mountains were

compared to data sets available for modern and ancient detrital sediments from the Snake River Plain (Geslin et al., 1999, 2002; Link et al., 2005; Beranek et al., 2006). We compared the coefficient values of cross-correlation, likeness, and similarity based on kernel density estimations (KDEs) of sample ages, and we performed Kuiper and Kolmogorov-Smirnov (K-S) tests on detrital zircon data sets using the DZStats v2.0 program for statistical comparison of detrital zircon age spectra (Saylor and Sundell, 2016). Cross-correlation, likeness, and similarity values can range between 0 and 1, with higher values representing a better fit between detrital zircon age spectra (Gehrels, 2000; Saylor and Sundell, 2016). K-S and Kuiper  $p$  values of  $<0.05$  indicate that two age spectra are from different sources, within 95% confidence (Press et al., 1986). Since the number of zircons analyzed from the Snake River Plain and Ringold Formation samples is typically  $<200$ , we used the mean Kuiper and K-S  $p$  values calculated from five trials of subsampling and comparison without replacement (Saylor and Sundell, 2016).

### Tephra Zircon Results and Interpretation

U-Pb zircon age results for tephra samples collected from the Saddle Mountains provide new age constraints on the timing and rate of sediment accumulation. The results of the individual LA-ICP-MS spot analyses for tephra samples are available in Tables DR2–DR6 (see footnote 1). From the hanging wall, we collected two tephra samples from section JR, which provided tephra ages in stratigraphic order (Figs. 5 and 9). For sample 15SM002, we calculated a concordia age of  $9.51 \pm 0.09$  Ma (mean square

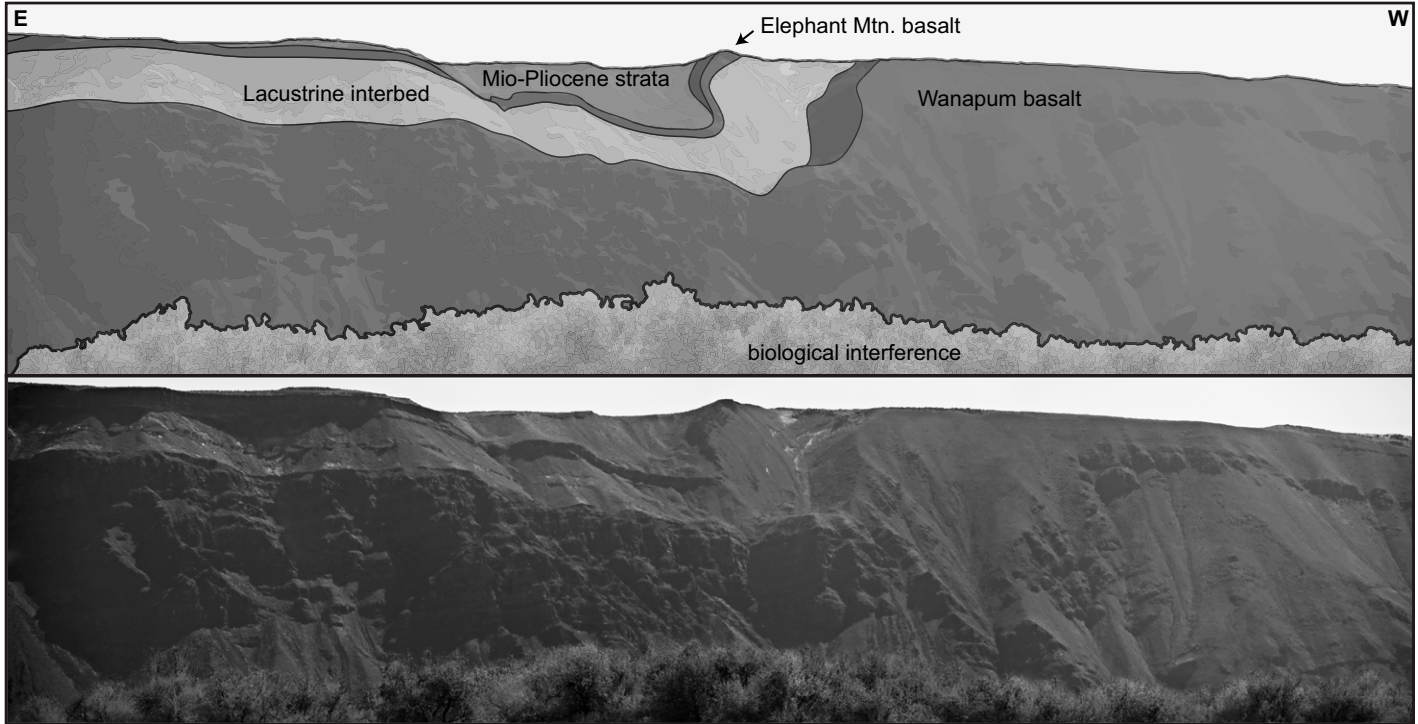


**Figure 8. Photograph and photo interpretation of a NW-trending, NE-vergent anticline in the hanging wall of the Saddle Mountains fault. Fold deforms the Columbia River Basalt Group strata as well as the Ringold strata and caliche (Fig. 6B). Cliff height along western extent of photo is approximately 330 meters. Mio.—Miocene. Photo by L. Staisch.**

of weighted deviates [MSWD] = 1.5) based on a group of 37 zircons out of the 48 analyses (Fig. 9A). For sample 16SM001, stratigraphically above 15SM002, we calculated an age of  $6.79 \pm 0.07$  Ma (MSWD = 1.3) from a coherent group of 78 zircons out of the 107 total analyses (Fig. 9B). As mentioned in the Appendix, the reference zircon material analyzed along with sample 16SM001 was 2.7% younger than the published age, and so we regard the concordia age of  $6.79 \pm 0.07$  Ma to be a minimum, albeit likely within ~3% of the true age of the sample.

For footwall samples, all ages occurred in stratigraphic order (Figs. 5 and 9). From the lowest sample collected in the Schoolhouse section (15SM006), we calculated a concordia age of  $9.51 \pm 0.14$  Ma (MSWD = 1.2) from a coherent group of 17 zircons out of the 35 concordant zircons analyzed (Fig. 9C). Stratigraphically above 15SM006, results from sample 15SM007 provided a concordia age of  $8.06 \pm 0.20$  Ma (MSWD = 1.4) based on a group of 21 zircons (Fig. 9D) from a total of 23 concordant analyses. Sample 15SM003 provided a concordia age of  $7.35 \pm 0.40$  Ma (MSWD = 2.2) based on a group of six concordant zircons (Fig. 9E). In total, 35 concordant zircon ages were measured for sample 15SM003. From the reworked tephra sample 15SM004, which was the highest tephra sample collected from the footwall, we

calculated a concordia age of  $3.48 \pm 0.11$  Ma (MSWD = 1.3) from the youngest five coherent analyses (Fig. 9F). In total, 137 zircons were dated, as this sample was analyzed as a detrital zircon sample.

Normalized relative probability plots for tephra samples indicate that samples 15SM002, 15SM006, 15SM007, and 16SM001 were minimally reworked, with the vast majority of single-crystal ages falling within a Neogene age peak (Fig. DR2 [see footnote 1]). Therefore, we interpret the calculated concordia dates for these samples to represent the timing of volcanic

deposition. The broader and less-defined young age peak for sample 15SM003 (Fig. DR2 [see footnote 1]) indicates that the calculated age may have been more affected by detrital contamination than others, and so we interpret the concordia age of  $7.35 \pm 0.40$  Ma to represent a maximum depositional age for this tephra. Similarly, for sample 15SM004, this sample was clearly reworked, and the majority of the zircons dated were detrital (Fig. DR3 [see footnote 1]). Thus, the  $3.48 \pm 0.11$  Ma concordia age calculated for the youngest five analyses represents a maximum depositional age.

**Figure 9 (on following page).** Concordia plots showing the U-Pb zircon age results for tephra interbedded within the Ringold Formation. On all plots, solid gray ellipses are the concordant and coherent group of zircons used to calculate the concordia age. Dashed ellipses are dated zircons that are not concordant, have high analytical errors, or are otherwise considered outliers. The thick black ellipse in each plot is the calculated concordia age. On each plot, we report the concordia age and  $2\sigma$  uncertainty, mean square of the weighted deviates (MSWD), and the number of zircons ( $N$ ) within the coherent group. (A) Results for sample 15SM002 from the hanging wall (lowermost sample from directly above the weathered basalt in the Jericho section). (B) Results from 16SM001, upper sample from near the top of the Jericho section. (C) Results from 15SM006, stratigraphically the lowest sample collected from the footwall (Schoolhouse section). (D) Results from 15SM007, the second lowest sample collected from the footwall (Schoolhouse section). (E) Results from 15SM003, collected just below the channel-fill marker bed in the footwall (Mathews Canyon section). (F) Result from 15SM004 of reworked tephra collected near the top of the footwall strata (Mathews Canyon section).

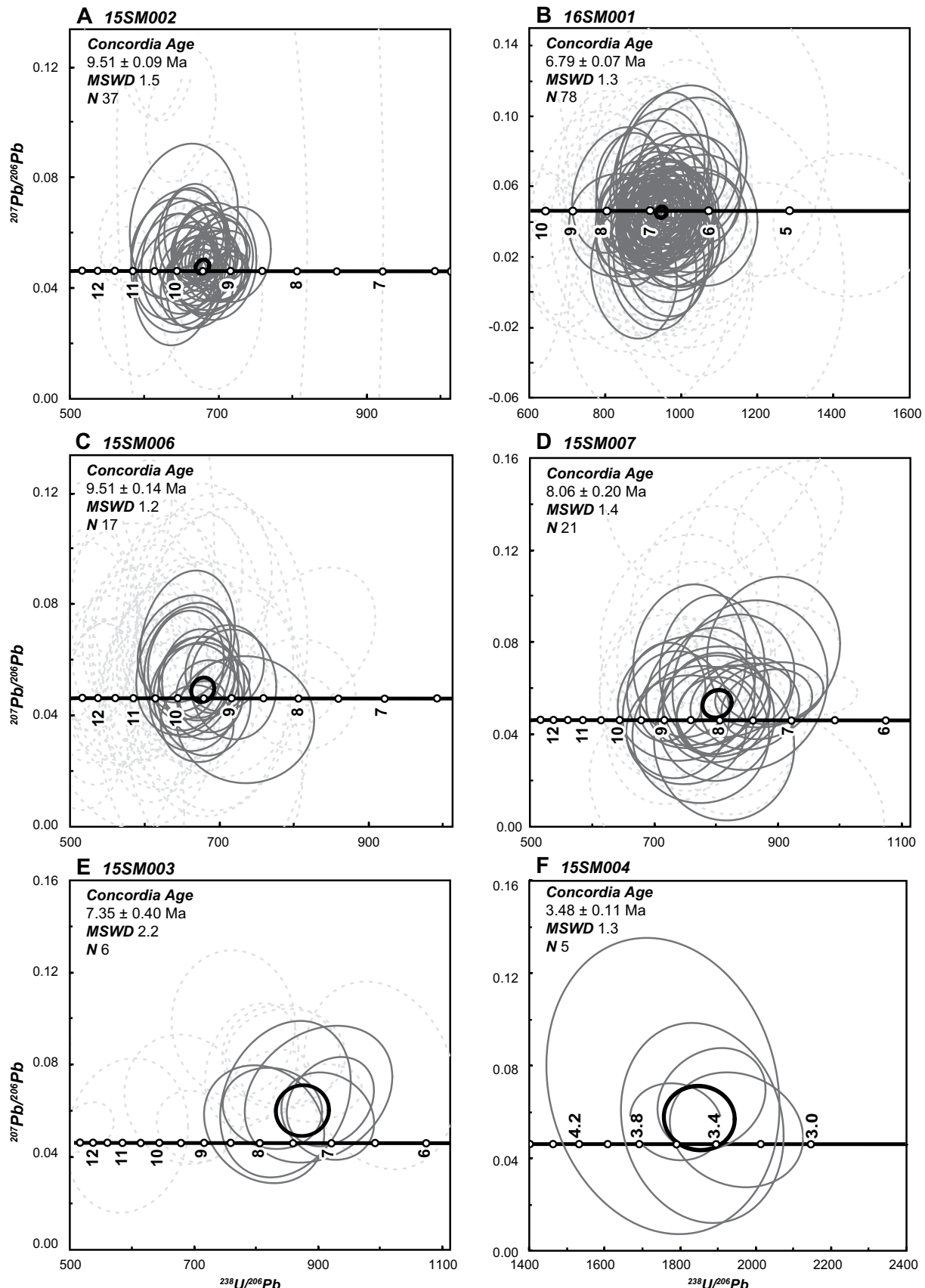


Figure 9.

From the similarity in tephra age and appearance of samples 15SM002 and 15SM006, we interpret these tephra to be correlated horizons across the hanging wall and footwall of the Saddle Mountains fault (Fig. 5). Our U-Pb zircon tephra ages of the lower Ringold Formation establish the age of the base of the unit as 9.51 Ma; the base of the formation is not exposed at the Taunton section and was difficult to date by magnetostratigraphy elsewhere (Packer and Johnson, 1979). The uppermost tephra sample from the footwall strata has an age of  $3.48 \pm 0.11$  Ma, whereas the uppermost tephra sample from the hanging wall is older at  $6.79 \pm 0.07$  Ma (Fig. 5). This may indicate that, in the hanging wall, deposition of the Ringold Formation ceased in the late Miocene and/or that the preservation of younger Ringold strata is less complete in the hanging-wall than in the footwall sections. In summary, our new geochronologic age constraints suggest that the Ringold Formation was deposited between 9.5 and 3.5 Ma. These data are supported by previous magnetostratigraphic analyses of the upper Ringold strata at the Taunton section (Figs. 2 and 7), where Packer and Johnson (1979) suggested lacustrine deposition during the Gilbert Epoch, from 3.596 to 6.033 Ma, using the time scale from Gradstein et al. (2012).

#### **U-Pb Provenance Results and Interpretation**

Since the rock exposed along the Saddle Mountains anticline is nearly uniformly basaltic, the range of zircon ages and presence of recycled metamorphic minerals indicate that the hanging wall was not uplifted above river level until after the cessation of predominantly conglomeratic deposition. Detrital U-Pb zircons ages for samples 15SM004 and 15SM013 range between 3.3 and 3368 Ma (Fig. DR2; Tables DR7–DR8 [see footnote 1]). As mentioned already, we interpret the concordant Pliocene zircon ages in 15SM004 to represent the timing of deposition and the older ages to represent reworked fluvial sands. In addition to zircon dating, we identified monazite, rutile, garnet, and multiple zircon habits during mineral separation of these samples, one of which was taken from the hanging-wall strata (Fig. 5). These minerals, particularly monazite, indicate that the lower Ringold strata sources material other than basalt, such as primary or reworked felsic igneous or metamorphic rocks.

For intersample comparison of detrital data sets from the Ringold strata and from the Snake River Plain (Geslin et al., 1999, 2002; Link et al., 2005; Beranek et al., 2006), the results for cross-correlation, likeness, similarity, Kuiper, and K-S tests are reported in Table DR9 (see footnote 1). The cross-correlation, likeness, and similarity values between the detrital zircon age spec-

tra measured in the Ringold strata (15SM004, 15SM013) are uniformly high ( $>0.75$ ), and the Kuiper and K-S *p* values are above 0.05 (Table DR9 [see footnote 1]). For intersample comparison of Ringold strata with modern and ancient river sands of the Snake River Plain, cross-correlation, likeness, and similarity values typically range between 0.1 and 0.8 (Table DR9 [see footnote 1]). Mean Kuiper and K-S *p* values range between 0.0 and 0.7 (Table DR9 [see footnote 1]).

Based on our analysis, we find that the source of the Ringold Formation did not change over the sampled interval and a subset of the Snake River Plain samples compares well with the Ringold Formation samples. As mentioned earlier, samples with mean K-S and Kuiper *p* values above 0.05 and with high coefficients of likeness, similarity, and cross-correlation are likely derived from the same source terrane (Saylor and Sundell, 2016). The threshold of what is considered a good comparison for likeness, similarity, and cross-correlation is somewhat arbitrary, and we chose a conservative value of 0.65. Several of the detrital zircon data sets have relatively few zircons ( $n < 100$ ) and require interpretation of intersample comparison coefficients with caution. Therefore, we only consider age spectra to be potentially derived from the same source terrane if both K-S and Kuiper *p* values are above 0.05, and all cross-correlation, likeness, and similarity coefficients are above 0.65. Based on these criteria, our results indicate that the only Snake River Plain samples that are statistically similar to our Ringold samples are modern Snake River (M5 and M6), the Pleistocene South Fork of the Snake River (P6), and the Pleistocene Bonanza Bar (P7; Fig. 10; Fig. DR3; Table DR9 [see footnote 1]).

The most abundant age population peaks that overlap between the Ringold and Snake River Plain samples are the Eocene Challis Volcanic Group and the Cretaceous Idaho Batholith, both of which are exposed primarily north of the Snake River Plain (Fig. 10; Fig. DR3 [see footnote 1]). The zircons older than 250 Ma that overlap between Snake River Plain and Ringold samples include Precambrian age groups such as Grenville zircons, which were possibly recycled from central Idaho or the Idaho-Wyoming thrust belt (Stewart et al., 2001), the Yavapai-Mazatzal, which may be recycled from conglomerates in western Wyoming (Janecke et al., 2000), and Wyoming Province zircons exposed in western Wyoming near the South Fork of the Snake River (Fig. DR3 [see footnote 1]; Link et al., 2005). Whether the similar age groups and statistical coefficients indicate that the Snake River itself flowed north of the Saddle Mountains during the Miocene is debatable (Fig. 10).

#### **Petrocalcic Horizon Dating**

We analyzed material from petrocalcic soil horizons collected from the Jericho and Schoolhouse stratigraphic sections for U-series age analysis to provide constraints on the timing of deformation along the Saddle Mountains. U-series dating of petrocalcic cements is based on the premise that the authigenic component precipitates from soil water capable of transporting U but not Th. The pure authigenic cement thus formed contains U with a  $^{234}\text{U}/^{238}\text{U}$  isotopic composition identical to that U dissolved in the soil water but no initial Th. With time,  $^{230}\text{Th}$  systematically increases due to in situ decay of  $^{234}\text{U}$ , such that a U-series age can be estimated by determining the  $^{234}\text{U}/^{238}\text{U}$  and  $^{230}\text{Th}/^{238}\text{U}$  activity ratios (AR). A detailed explanation of sample preparation and methods for U-series analysis is available in the Appendix.

Sample 15SM011 consists of calcified roots (rhizoliths) collected from the uppermost petrocalcic horizon exposed in the footwall strata (SH; Figs. 5, 6D, and 11A), which is undeformed at the site of collection but possibly correlative to the faulted horizons described in previous paleoseismic research along the Saddle Mountains fault (West et al., 1996). Samples 16SM002 and 16SM003 were collected from the uppermost petrocalcic horizon exposed in the hanging-wall strata (JR; Fig. 5), which is over 80 cm thick and has been tilted  $67^\circ$  at the site of collection (Fig. 6B). 16SM002 was collected from the lower portion of this calcic horizon, where the material is more massively cemented, and 16SM003 was collected from the uppermost beds, where thinner pedogenic rinds formed on the undersides of basaltic clasts (Figs. 11B and 11C).

#### **U-Series Results and Interpretations**

The U-series analysis of petrocalcic horizons and calcified rhizoliths provides the timing of calcification, which we used to interpret the timing of faulting and folding along the Saddle Mountains. Sample 15SM011, collected from the upper portion of the footwall strata, was not deformed at the site of collection but is from the same upper caliche unit faulted in paleoseismic trenches (Fig. 2; West et al., 1996). We analyzed three root casts, and age results range between 152 and 156 ka. Ages are within uncertainty of each other and provide a robust weighted mean age of  $153.2 \pm 3.8$  ka (Fig. 11; Table DR10 [see footnote 1]). We interpret these results to suggest that this horizon was calcified 153 k.y. ago and that earthquake activity along the Saddle Mountains fault deformed the caliche exposed in paleoseismic trenching more recently (West et al., 1996).

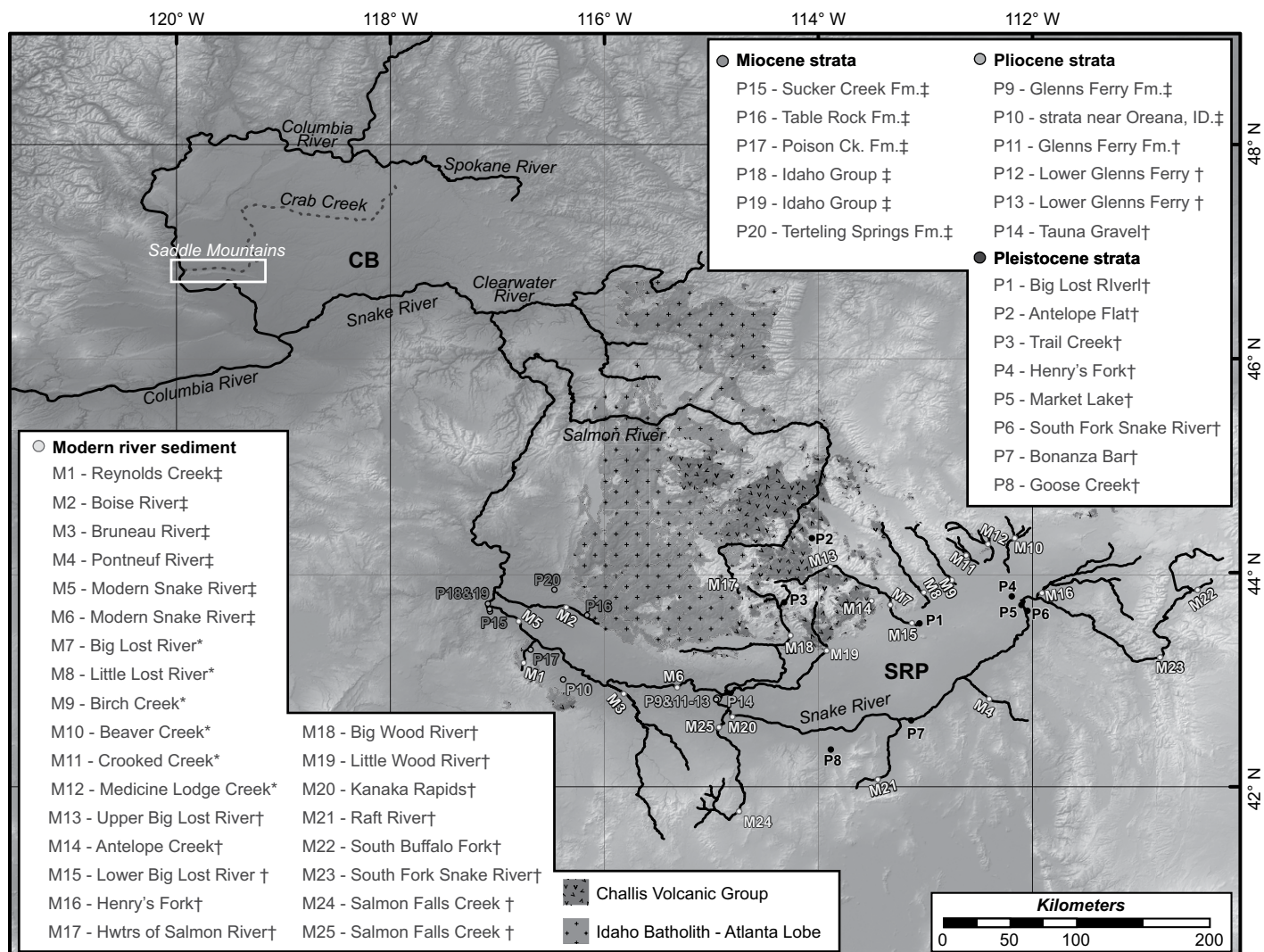


**Figure 10.** Geomorphic map of the Columbia Basin (CB) and Snake River Plain (SRP). Major rivers are shown in black and labeled. The mapped locations of the Atlanta lobe of the Idaho Batholith and the Challis Volcanic Group are shown in patterned shades of gray (Bond et al., 1978; Johnson and Raines, 1995). Sites where detrital zircon samples have been analyzed are indicated by light gray for modern river samples, black for Pleistocene-aged deposits, medium-light gray for Pliocene strata, and medium-dark gray for Miocene strata. In the legend, the references for each sample source are indicated by \* for Geslin et al. (1999, 2002), † for Link et al. (2005), and ‡ for Beranek et al. (2006). Values of statistical comparisons (similarity, likeness, and Kolmogorov-Smirnov [K-S] test) between Saddle Mountains and Snake River Plain detrital samples are available in Table DR9 (see text footnote 1). Digital elevation model (DEM) and derivative hillshade map are from 90 m data (<http://srtm.csi.cgiar.org/>).

Samples 16SM002 and 16SM003 were collected from the same petrocalcic horizon in the hanging wall of the Saddle Mountains fault, and they are distinguished by the nature of calcite formation: 16SM002 is from the massive calcite cement, whereas 16SM003 contains basaltic clasts with calcite rinds (Figs. 11B and 11C). Overall, the results from these samples are not as straightforward as 15SM011, with several subsamples not providing interpretable ages due to excess  $^{230}\text{Th}$  values or high  $^{232}\text{Th}$  values (Table DR10 [see footnote 1]). For the subsamples that provided reasonable results, ages

ranged from 79 to 434 ka for sample 16SM002, and from 45 to 195 ka for sample 16SM003 (Fig. 11). The large range in age results could suggest one of two things: (1) Samples have been diagenetically altered, leading to a depletion of U and preferential enrichment of Th, in which case the calculated ages are not geologically meaningful. (2) Multiple stages of calcite growth have lead to multiple age groups in U-series data.

To determine which scenario is most likely, we compared the calculated U-series ages with initial  $^{234}\text{U}/^{238}\text{U}$  values. Individually, samples

16SM002 and 16SM003 do not show a particularly strong correlation between age and U ratios; however, taken together, we find that the subsamples with low initial  $^{234}\text{U}/^{238}\text{U}$  (between 1.05 and 1.1) are younger and cluster around 100 ka. The remaining subsamples have higher ratios, between 1.3 and 1.5, and older ages (>200 ka). Given the correlation evident in the combined sample ages, we suggest that the sampled horizon has undergone several stages of calcite growth. The age of the first stage is somewhat poorly constrained between 200 and 400 ka, and results show high initial  $^{234}\text{U}/^{238}\text{U}$

values. The second pedogenic event, with lower  $^{234}\text{U}/^{238}\text{U}$  values, likely occurred between 100 and 90 ka. The difference in U composition is perhaps due to different climatic conditions and weathering rates during the time of pedogenic carbonate formation.

Deformation of the uppermost petrocalcic horizon at JR (Fig. 6B) is due to folding of the hanging wall (Fig. 8), possibly accommodating motion along a lateral ramp at depth. Prior to calcification, the original material of hanging-wall and footwall samples consisted of fine loess and was likely friable. The results from samples 16SM002 and 16SM003 show two age groups between 100 and 90 ka and 400 and 200 ka. From these data, we suggest that deformation of the horizon postdated the oldest stage of calcification and is therefore more recent than 200 ka.

## STRUCTURAL CROSS SECTIONS

The form of the Saddle Mountain anticline varies along strike, and this variation may be strongly influenced by changes in the underlying fault at depth (Suppe, 1985; Rowan and Linares, 2000; Allmendinger and Shaw, 2000; Wilkerson et al., 2002). Thus, we constructed two cross sections, A-A' and B-B', to investigate the effect of along-strike changes in fold, and likely fault, geometry (Fig. 2). Both cross sections have a present-day length of 14 km and strike N4°W, parallel to the inferred direction of maximum convergence. To constrain our work, we used geological and geophysical data and combined traditional cross-section line-balancing (Dahlstrom, 1969) with forward modeling of geophysical anomaly data.

Geologic constraints used in cross-section construction include new and published structural measurements near cross-section transects (Fig. 2; Reidel, 1988), isopach data for stratigraphic thicknesses of Columbia River Basalt Group strata (Reidel, 1984), and logged stratigraphy in nearby boreholes BN 1–9, AF 1–6, and Brown 7–24 (Fig. 1; Fig. DR1 [see footnote 1]; Wilson et al., 2008; Czajkowski et al., 2012). Borehole locations span the full length of the structural transects, and borehole measurements reach up to 5.3 km depth, including both Columbia River Basalt Group flow thickness as well as unit thicknesses of the underlying Fifes Peak/Ohanapecoh, Wenatchee, and Roslyn Formations. Isopach data indicate thinning of several Saddle Mountains Basalt members (Reidel, 1984), which is honored in our cross sections, while basalt members remain at constant thickness.

Geophysical controls on our structural cross sections include seismic-reflection data and

high-resolution aeromagnetic anomaly data (Figs. 2 and 12). The seismic profile that elucidates the Saddle Mountains fault geometry was purchased by the U.S. Geological Survey and interpreted previously by Casale and Pratt (2015). Seismic reflections interpreted as bedding orientations reach depths to 8–10 km. The upper several kilometers of the seismic line are particularly difficult to image because of the Columbia River Basalt Group basalt stratigraphy; however, interpretable reflectors are apparent in deeper horizons (>2 km depth). Aeromagnetic data, on the other hand, are extremely informative for structures in the Yakima fold province because of the highly variable magnetic properties of rock types within the region. These include highly magnetized basalts, with both normal and reverse polarity, and essentially nonmagnetic overlying and underlying strata (Blakely et al., 2011). The data shown in Figure 12 were acquired in 2008 and 2009 by private consultants under contract to the U.S. Geological Survey. Blakely et al. (2011) provided a full description of data acquisition and processing procedures. In addition to providing constraints on the cross-section results, these aeromagnetic data were used to modify the mapped trace of the Saddle Mountains fault where field observations were lacking by tracing contours in strong horizontal gradients calculated from the magnetic anomaly data (Figs. 2 and 12).

## Methods

The surface geology along transects A-A' and B-B' were matched to the geologic mapping of Reidel (1988) and supplemented with new bedding orientations where structural data were originally sparse (Fig. 2). These data were entered into Oasis Montaj, a program for modeling geophysical data, along with the aeromagnetic data and a 10-m-resolution digital elevation model of the Saddle Mountains anticline. For our analysis, we used the 100-m-resolution total field magnetic anomaly

data, where the International Geomagnetic Reference Field, updated to the time of flight, was subtracted from the original total field measurements (Fig. 12). Further details on aeromagnetic data processing are available in Blakely et al. (2011). For basaltic flows and overlying strata, we compiled paleomagnetic data and calculated the weighted mean of spherical quantities for inclination and declination in each flow (Packer and Johnson, 1979; Choiniere and Swanson, 1979; Hooper et al., 1979; Wells et al., 1989). For the sub-basaltic strata, we adopted magnetic parameters from Blakely et al. (2011). Table 2 includes information on the magnetic parameters used for each unit.

Magnetic anomaly data were extracted along each cross-section transect for forward modeling in Oasis Montaj. As cross sections were constructed, the resulting magnetic anomalies were calculated and compared to measured magnetic anomaly data. Unit thicknesses were kept constant unless isopach data suggested otherwise (Reidel, 1984), and bedding orientations were matched to available structural data. The upper and lower contacts of each unit were line-balanced using the sinuous bed method (Dahlstrom, 1969). Exceptions to this include the contact between the Pomona and Huntzinger flows and the base of the Roslyn Formation. The Pomona and Huntzinger flows both thin toward the crest of the Saddle Mountains anticline and are not observed to the north of the anticlinal crest, and therefore cannot be line balanced with the other contacts. We did not line-balance the basal contact of the Roslyn Formation because seismic-reflection data indicate that bedding in the Roslyn Formation dips more steeply than overlying strata and likely experienced more shortening prior to deposition of the Wenatchee Formation (Casale and Pratt, 2015). Furthermore, borehole data do not penetrate into deeper strata, and so the base of the Roslyn Formation and/or top of the basement are/is not well constrained near the Saddle Mountains (Fig. DR1 [see footnote 1]).

**Figure 11 (on following page).** U-series age results for aliquots of petrocalcic horizons. All ages reported are for individual aliquots with  $2\sigma$  analytical uncertainty. Aliquots with excess Th do not provide an interpretable age due to detrital  $^{230}\text{Th}$  contamination or diagenetic depletion of U. (A) Results for sample 15SM011, aliquots A–C, collected from the upper caliche horizon in footwall Schoolhouse section. (B) Results for sample 16SM002, aliquots A1–A2, B1–B3, C1–C2, D1, E1–E2, and F1–F2, collected from the thick upper calcrete in the hanging-wall Jericho section. (C) Results from sample 16SM003, aliquots A1–A3, B1–B3, C1, D1–D3, and G1–G2 collected from the same location as 16SM002. (D) Results for all samples plotted on an isochron age plot. Data points with gray outlines are aliquots that did not produce an interpretable age or uncertainty. The inset shows the weighted mean age derived for sample 15SM011 (MSWD—mean square of weighted deviates).

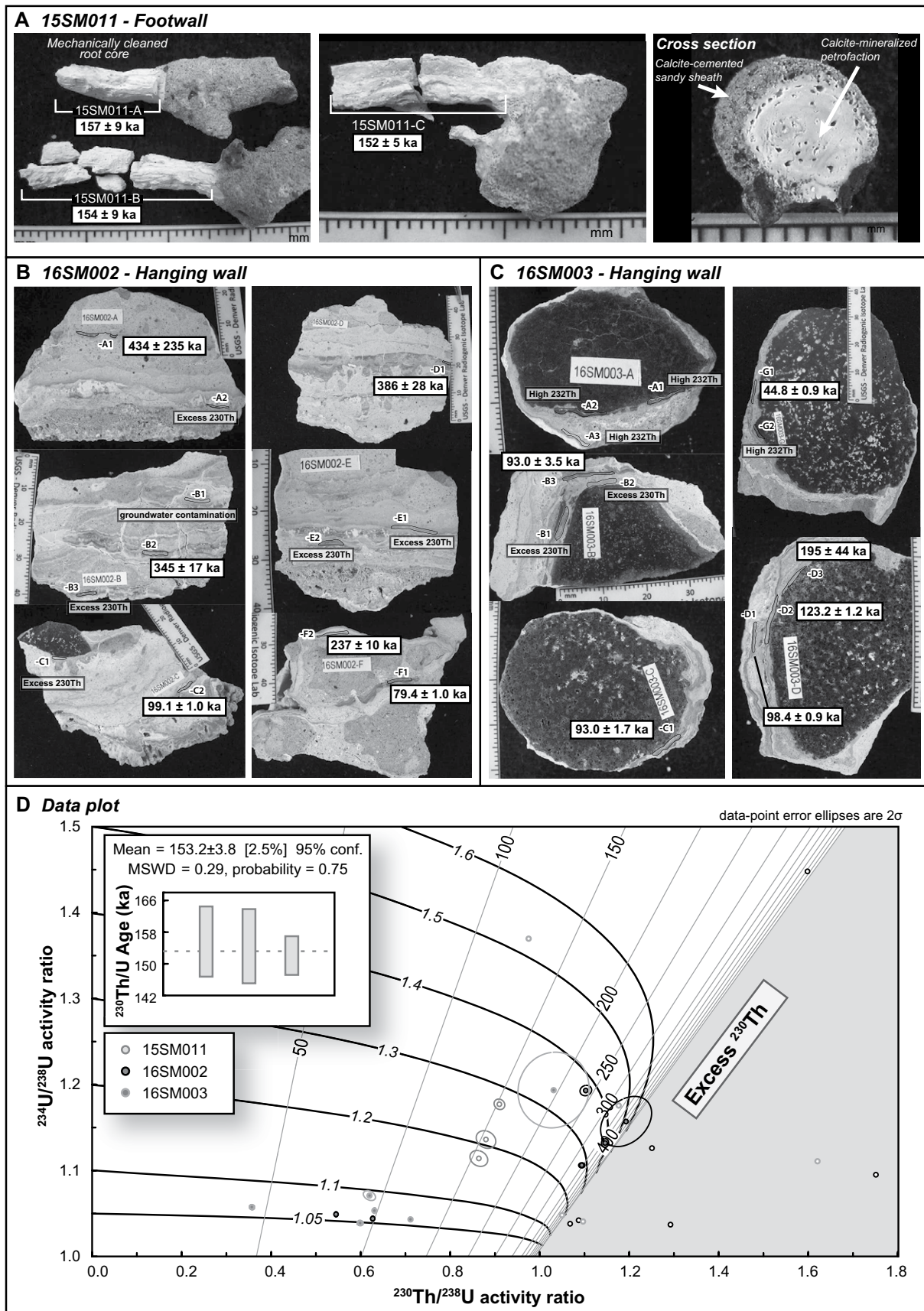
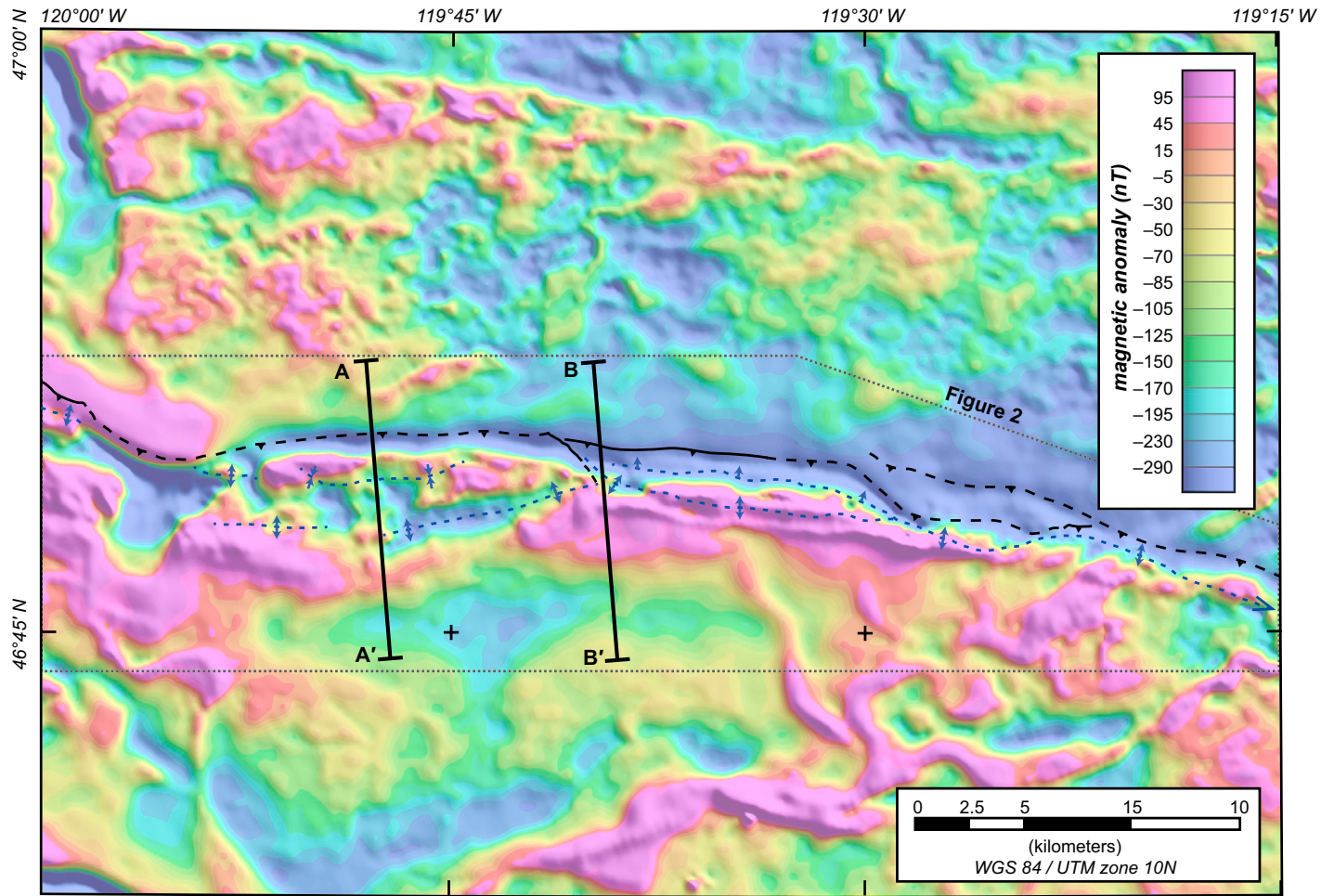


Figure 11.



**Figure 12.** Map of 100-m-resolution total field magnetic anomaly data measured over the Saddle Mountains anticline. More positive magnetic anomalies are shown in warm colors, and negative anomalies are shown in cool colors. Basic structures and cross section transects A-A' and B-B' are plotted for reference. Fault traces are from Figure 2, and were modified from Reidel (1988) based on new field observations, cross section results, and strong horizontal gradients from the magnetic anomaly data. The main differences in fault trace location are to the west of Smyrna bench, where the fault trace is obscured by alluvial fans (Fig. 2). WGS 84—World Geodetic System 1984; UTM—Universal Transverse Mercator.

TABLE 2. GEOLOGIC UNITS AND THEIR MAGNETIC PARAMETERS USED FOR GEOPHYSICAL MODELING

Rock unit formation	Member	Age (Ma)	$\rho$ (g/cm <sup>3</sup> )	$\chi$ (emu/cm <sup>3</sup> )	Mr (emu/cm <sup>3</sup> )	Magnetization	$\Delta\rho$ (g/cm <sup>3</sup> )	Declination (°)	Inclination (°)
Saddle Mountains	Qt loess	—	Qt	2.17	0.0000	0.0000	—	-0.50	—
	Ringold	—	3.0–9.5	2.47	0.0000	0.0000	All	-0.20	2.40
	Elephant Mtn	10.0–10.5	2.67	0.0005	0.0020	N,T	0.00	81.20	-14.43
	Pomona	12	2.67	0.0005	0.0020	R	0.00	198.04	-64.90
Wanapum	Asotin	13	2.67	0.0005	0.0020	N	0.00	352.42	72.89
	Priest Rapids	14.5	2.67	0.0005	0.0020	R	0.00	190.50	-64.90
	Roza	—	2.67	0.0005	0.0020	R,T	0.00	198.08	-27.81
	Frenchman Springs	15.3	2.67	0.0005	0.0020	N,T	0.00	26.46	51.65
Grande Ronde	Sentinel Bluffs (N2)	15.5–15.7	2.67	0.0005	0.0025	N	0.00	355.44	65.77
	Schwana (R2)	15.7–15.9	2.72	0.0005	0.0025	R	0.05	219.02	-71.47
	GR-N1	15.9–16.1	2.77	0.0005	0.0025	N	0.10	354.59	57.63
	GR-R1	16.1–16.9	2.78	0.0005	0.0025	R	0.11	170.78	-66.31
Ellensburg	—	—	2.57	0.0000	0.0000	All	-0.10	—	—
Wenatchee	—	>44.5	2.57	0.0000	0.0000	All	-0.10	—	—
Roslyn	—	45–48	2.57	0.0000	0.0000	All	-0.10	—	—

Note: Paleomagnetic measurements were compiled from Packer and Johnson (1979); Choiniere and Swanson (1979); Hooper et al. (1979); and Wells et al. (1989). Qt—Quaternary;  $\rho$ —density;  $\chi$ —magnetic susceptibility; Mr—remnant magnetization; R—reverse magnetic polarity; N—normal magnetic polarity; T—transitional magnetic polarity.

## Cross-Section Results and Interpretations

The aeromagnetic data extracted across each cross-section transect show a notable along-strike variability in magnetic anomalies that correlates to a difference in the surface geology and structure at depth, and cross sections A-A' and B-B' (Fig. 13) are best fits to the geologic and geophysical data. From the finalized cross sections, we calculated an original length for A-A' of 15.33 km, giving an overall shortening of 1330 m (9% shortening) since deposition of the Columbia River Basalt Group. For cross section B-B', we calculated an original length of 14.96 km and an overall shortening of 960 m (6% shortening) since deposition of the Columbia River Basalt Group. At the projected location of BN 1–9 on cross section B-B', we estimated a fault depth of 2300 m and an ~450-m-thick repeated section of basalt. These values overlap with estimates of fault depth from fractured rock mass and repeated section from basalt geochemistry (Reidel et al., 1989a), providing independent support for our cross-section modeling results. Steeper bed orientations in Eocene strata suggest pre-Miocene deformation on the Saddle Mountains anticline; however, the aeromagnetic data, isopach data, and the uniform shortening along each line-balanced layer suggest that the majority of deformation recorded in the Columbia River Basalt Group strata, and possibly the Oligocene strata, postdated the youngest basalt flow, the 10–10.5 Ma Elephant Mountain Member.

While shortening in each balanced layer is uniform, the magnitude of slip increases with the age of the unit, from which we infer that the Saddle Mountains anticline is a fault-propagation fold (Suppe, 1985; Suppe and Medwedeff, 1990; Mitra, 1990), similar to other Yakima folds (Miller, 2014). Thus, the amount of slip preserved in the upper units is an underestimate for the total Miocene to present slip history. To avoid underestimating total slip, and in turn slip rate, we measured the total offset from the oldest uniformly shortened unit, the Wenatchee Formation. Our estimates for total slip since 10.5–10.0 Ma are 1712 m along A-A' and 1178 m along B-B'.

Given our shortening and slip estimates, our structural models suggest that there is a westward-increasing slip gradient along the Saddle Mountains fault. The slip gradient is consistent with large-scale, long-term clockwise rotation in the U.S. Pacific Northwest (Wells et al., 1998; Wells and McCaffrey, 2013). Clockwise rotation and westward-increasing N-S strain rates are ongoing, as evident from modern global positioning system (GPS) measurements in the Yakima fold province (McCaffrey et al., 2013,

2016). Our new cross sections provide evidence that clockwise rotation could be manifest along a single structure, and not just along a larger array of structures.

While the upper-crustal structure of the Saddle Mountains varies along strike, the Saddle Mountains fault likely merges at depth to a common fault plane geometry. In our structural model, this occurs at depths between 6 and 7 km (Figs. 13 and 14). We posit that a lateral ramp, or perhaps multiple lateral ramps, accommodates the along-strike variation (Fig. 14). Several lines of evidence support this interpretation. First, minor apparent right-lateral offset on the Smyrna fault, near the Mathews Canyon section (Fig. 2), displaces Columbia River Basalt Group flows by tens of meters, so there has certainly been some amount of oblique dextral motion on fault step-overs. Furthermore, hanging-wall fold axes near the Jericho and Pinnacle sections (Fig. 8) are orthogonal to the large-scale trend of the Saddle Mountains anticline and may indicate the presence of a lateral ramp at depth (Wilkerston et al., 2002).

## DISCUSSION

### Timing and Rates of Deformation and Landscape Evolution

#### *Miocene–Pliocene Structural and Stratigraphic Evolution of the Saddle Mountains*

Using the new and published stratigraphic, structural, and geochronologic constraints, we reconstructed the geologic history of the Saddle Mountains. The onset of deformation likely predicated the late Eocene–Oligocene deposition of the Fifes Peak/Ohanapecosh and Wenatchee Formations, based on the steepening of bedding orientations within the Roslyn Formation (Casale and Pratt, 2015). Based on the uniform magnitude of shortening preserved in post-Roslyn Formation strata, we infer that there was paucity of deformation from 45 Ma until at least 10 Ma along the Saddle Mountains anticline. Slight thinning of several basalt flows near the crest of the Saddle Mountains anticline may suggest that minor anticlinal growth occurred between ca. 16 and 11 Ma (Reidel, 1984), but we establish from our cross section results that deformation at this time was relatively minor compared to the overall shortening accommodated along the Saddle Mountains anticline. Our new tephra U-Pb zircon age results indicate that the onset of Ringold Formation deposition was ca. 9.5 Ma and that deposition ceased shortly after 3.5 Ma. The initiation of debris-flow and mudflow deposition in the lower Ringold Formation at 9.5 Ma signals relief generation across

the Saddle Mountains by this time. We therefore suggest the onset of renewed deformation along the Saddle Mountains anticline between 10 and 9.5 Ma. Stratigraphic observations and tephra dating indicate that deposition of debris flows and mudflows continued throughout the late Miocene and into the Pliocene (until at least 3.5 Ma), which we interpret as continued anticlinal growth, relief generation, and hill-slope erosion.

Stratigraphic observations also allow us to characterize Miocene–Pliocene deformation along the Saddle Mountains anticline. The upper boundary of conglomerate-dominated strata in the hanging-wall sections is marked by a fluvial channel-fill horizon, below which we find detrital zircon grains with distal provenance similar to that of the Snake River Plain. This indicates that the hanging wall remained at river level for some time. However, the strata in the hanging wall and footwall become dissimilar after the fluvial channel-fill horizon. In the footwall, there is a shift from dominantly conglomeratic deposition to dominantly lacustrine deposition with interbedded mudflow and debris-flow facies (Fig. 5), whereas in the hanging wall, lacustrine strata are absent (Fig. 5). We infer that the hanging wall was uplifted above lake level by the time lacustrine deposition initiated and that the appearance of lacustrine strata in the footwall suggests that rivers were diverted away from the north side of the Saddle Mountains.

Concurrent with the lithostratigraphic shift, the footwall strata change from displaying fanning bedding dip orientations to displaying uniformly subhorizontal bedding (Fig. 4). Fanning dips we observed in the lower Ringold Formation are typical of growth strata (Suppe et al., 1992) and provide further evidence for syndepositional deformation in the footwall sections. The change to subhorizontal bedding suggests that the footwall was no longer tilted during deposition. We therefore suggest that the change from fanning to subhorizontal dips represents the time at which the Saddle Mountains fault propagated to the surface, otherwise termed a fault breakout (Allmendinger, 1998).

### *Age Estimate for Channel-Fill Marker Bed*

From our stratigraphic observations of the Ringold Formation near the Saddle Mountains anticline, we identified a unique channel-fill horizon present in the majority of our measured sections (Fig. 5). Estimating the age of this horizon is essential for understanding the deformation history of the Saddle Mountains anticline for two reasons: First, this horizon, along with the 10.5–10.0 Ma Elephant Mountain Member, allows us to estimate the timing and rate of deformation (further discussed below).

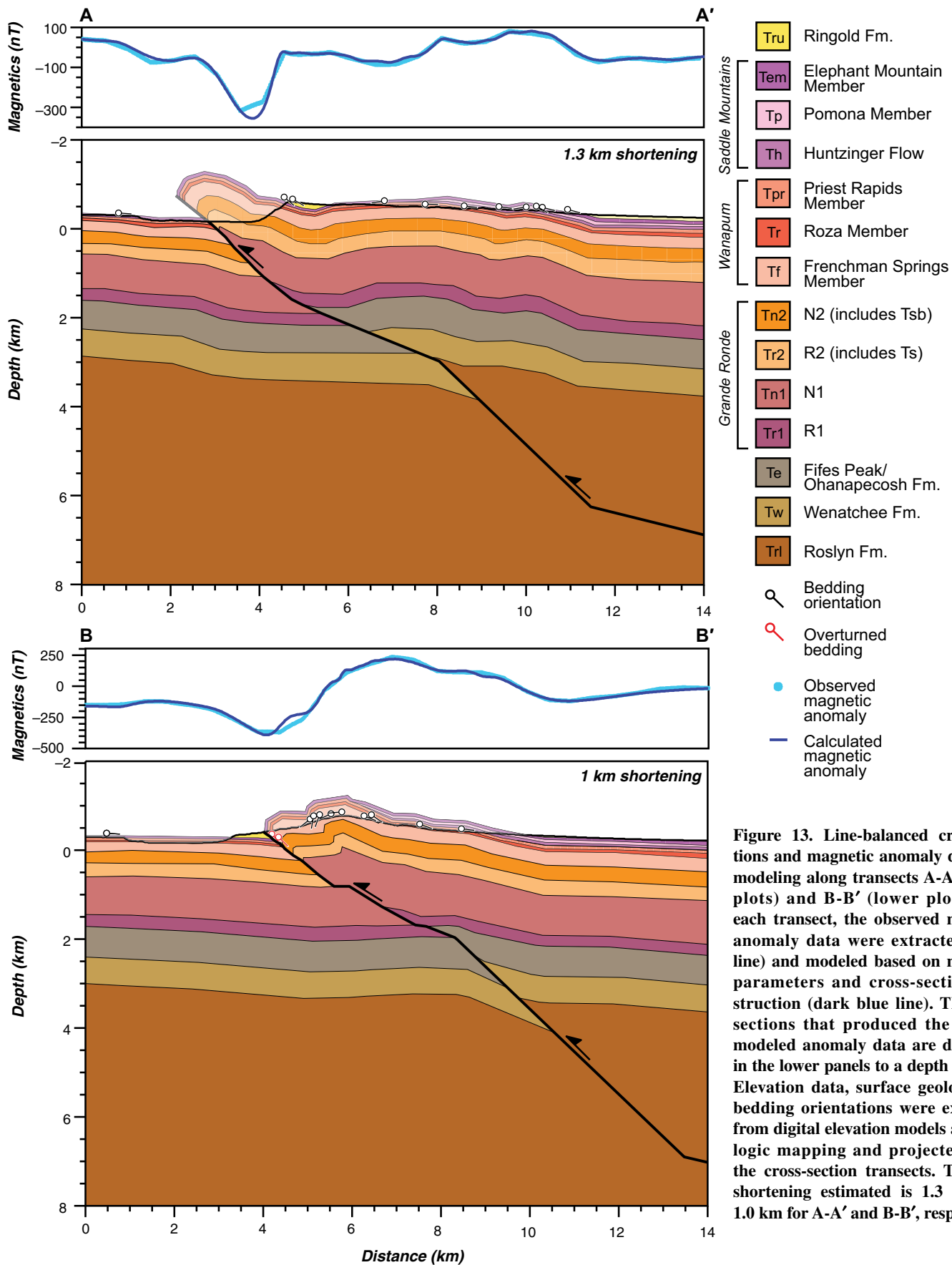
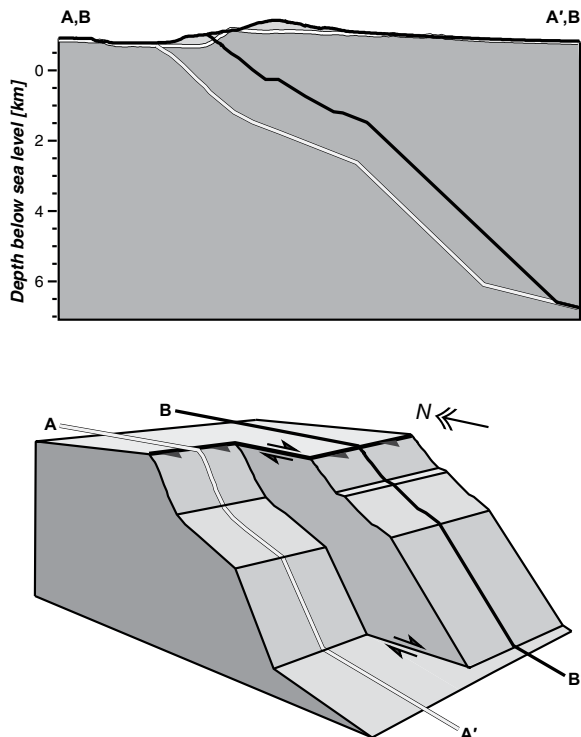


**Figure 13.** Line-balanced cross sections and magnetic anomaly data and modeling along transects A-A' (upper plots) and B-B' (lower plots). For each transect, the observed magnetic anomaly data were extracted (cyan line) and modeled based on magnetic parameters and cross-section construction (dark blue line). The cross sections that produced the best-fit modeled anomaly data are displayed in the lower panels to a depth of 8 km. Elevation data, surface geology, and bedding orientations were extracted from digital elevation models and geologic mapping and projected along the cross-section transects. The total shortening estimated is 1.3 km and 1.0 km for A-A' and B-B', respectively.

**Figure 14. Comparison of cross-sections A-A' and B-B'.** The upper diagram shows the cross sections overlain over each other, where the Saddle Mountains fault and topography along A-A' and B-B' are depicted in white and black, respectively. The lower diagram shows a schematic oblique block diagram of a lateral ramp accommodating along-strike variation in the Saddle Mountains fault. In this model, the lateral ramp would accommodate a component of right-lateral motion.



Second, this horizon forms the boundary between the lower Ringold Formation, where beds have fanning dips typical of growth strata (Suppe et al., 1992), and the upper Ringold Formation, where strata are subhorizontal (Fig. 4). Thus, the marker bed age provides an important constraint on the timing of fault breakout (Allmendinger, 1998).

To estimate the age of the marker bed, we assessed the tephra ages from the footwall strata and their relative stratigraphic positions. Given the linear relationship between stratigraphic position and tephra age, we were able to fit a simple linear regression through this data set and calculate that the channel-fill marker bed was deposited at  $6.81 \pm 0.27$  Ma (Fig. 15). We suggest, then, that the Saddle Mountains fault propagated to the surface soon after the deposition of the ca. 6.8 Ma marker horizon. Fault breakout at this time provides evidence of a tectonic mechanism for the dramatic change to dominantly lacustrine strata in the upper Ringold Formation. We propose that propagation of the Saddle Mountains fault to the surface ca. 6.8 Ma may have diverted the fluvial system, stratigraphically represented in the lower Ringold Formation, away from the actively growing anticline, creating a shallow lake system near the Saddle Mountains that persisted until 3.5 Ma. Based on the lack of lacustrine strata in the hanging wall (Fig. 5), we infer that enough relief was generated across the anticline after fault breakout to preclude lacustrine deposition in the hanging-

wall sections. Additionally, while the estimated 6.8 Ma age for the marker bed and the  $6.79 \pm 0.07$  Ma age for the uppermost hanging-wall tephra (16SM001) are within uncertainty, the lack of channel-fill deposition in section JR precludes our correlation between footwall strata and hanging-wall strata at JR (Fig. 5). The absent marker bed in the JR section may be from lack of preservation or from localized relief above river level at ca. 6.8 Ma. The proximity

of section JR to a small anticlinal crest in the hanging wall provides a mechanism for localized relief at this particular locality (Fig. 2).

#### Relief Generation and Spatiotemporal Variation in the Deformation Rate

The presence of two marker beds in Miocene basaltic and suprabasaltic strata gives us the unique opportunity to estimate the magnitude of structural relief generated across the Saddle Mountains anticline over time (Suppe et al., 1992). We reconstructed the magnitude of structural relief generated by 6.8 Ma using the difference in the thickness of strata between the 10.5–10.0 Ma Elephant Mountain Member and the 6.8 Ma marker bed (Fig. 16). The stratigraphic separation between the Elephant Mountain Member and the channel-fill marker bed in the footwall ( $T_F$ ) varies from 50 to 54 m, which we average to 52 m (Figs. 5 and 16). The stratigraphic separation between these two marker horizons in the hanging wall ( $T_H$ ), on the other hand, ranges between 10 and 29 m (Fig. 5). The Pinnacle section (PN) is nearly identical in lithostratigraphy but more complete than the nearby Duct Tape section (DS), from which we posit that localized relief has reduced the stratigraphic separation in section DS (Fig. 5). We therefore only considered stratigraphic separations between the Elephant Mountain Member and the channel-fill marker bed ( $T_H$ ) from sections PN and FL in the hanging wall, which are 24 and 29 m, respectively (Fig. 5). From the difference between  $T_F$  and  $T_H$ , we calculated that, between 10.5–10.0 Ma and 6.8 Ma, 28 m of structural relief were generated on the Saddle Mountains anticline at PN, and 23 m of structural relief were generated along the Saddle

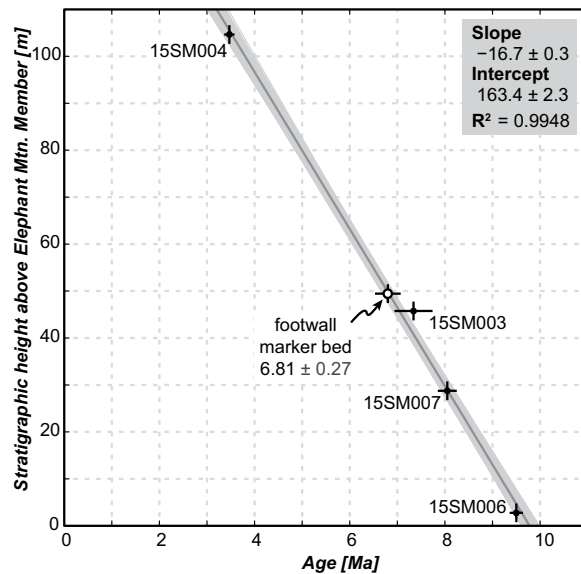
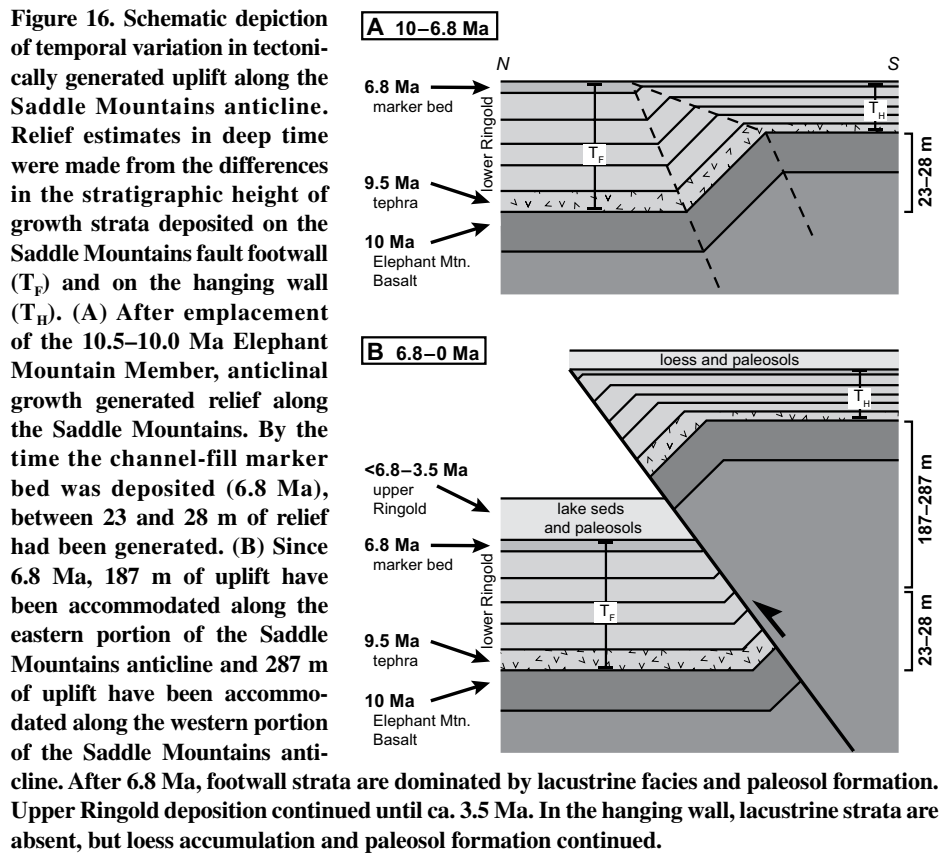


**Figure 15. Sediment accumulation rate of the Ringold Formation in the footwall of the Saddle Mountains fault estimated using a linear regression of U-Pb zircon tephra ages and stratigraphic position of the tephra. The age of the marker bed horizon estimated using this sediment accumulation rate is  $6.8 \pm 0.35$  Ma.**



Mountains anticline near FL (Fig. 16). The magnitude of structural relief generated across the Saddle Mountains anticline since 6.8 Ma is much greater, varying from 187 m in the east (PN) to 287 m in the west (JR; Fig. 16).

The structural relief generated, equivalent to relative rock uplift, along the Saddle Mountains anticline over these two periods of time allows us to calculate the rate of deformation and how it varies spatially and temporally. Between 10.5–10.0 Ma and 6.8 Ma, the rate of relative rock uplift along the Saddle Mountains anticline was  $<0.01 \text{ mm yr}^{-1}$ . The average rate after 6.8 Ma is up to six times greater than the previous rate, ranging between  $0.04 \text{ mm yr}^{-1}$  in the west and  $0.02 \text{ mm yr}^{-1}$  in the east. The spatial variation in uplift rates is consistent with the results from our structural cross sections that show an overall westward-increasing slip gradient along the Saddle Mountains fault. Given the magnitude of shortening and slip we established in our cross sections along the Saddle Mountains fault (Fig. 13), we calculated that the shortening rate between 10.5–10.0 Ma and 6.8 Ma was  $0.03\text{--}0.04 \text{ mm yr}^{-1}$  and that the rate of slip during this same time was  $0.04\text{--}0.05 \text{ mm yr}^{-1}$ . Since 6.8 Ma, the shortening rate increased to  $0.18 \text{ mm yr}^{-1}$  in the west and  $0.12 \text{ mm yr}^{-1}$  in the east. For this same time period, the slip rate increased to

$0.23 \text{ mm yr}^{-1}$  in the west and  $0.15 \text{ mm yr}^{-1}$  in the east. Because the rock uplift rates between 10.5–10.0 Ma and 6.8 Ma are low and within uncertainty of each other, we are unable to assess from our data whether this E-W deformation gradient was established before 6.8 Ma.

Previous studies on rotation of the magmatic arc indicated that clockwise rotation of the U.S. Pacific Northwest was established by 16 Ma (Wells and McCaffrey, 2013). Since the westward-increasing cumulative deformation along the Saddle Mountains anticline mimics the long-term, regional clockwise rotation, this could suggest that the slip gradient along the Saddle Mountains fault was established early in the uplift history. If the slip gradient has been a consistent and long-term character of the Saddle Mountains, we would expect the geomorphology across the Saddle Mountains anticline to be similarly adjusted to the deformation rate. Another possibility is that the slip gradient along the Saddle Mountains anticline is a product of eastward lateral fold propagation, from which we would expect to see an eastward decrease in drainage density and ridge dissection, as this would be a structurally and geomorphically young region of the fold (Keller et al., 1999). Geomorphically, however, the landscape along the western portion of the Saddle Mountains ap-

pears younger than the eastern portion. Therefore, we suggest that the decreased drainage density and ridge dissection along the western portion of the fold may indicate that the landscape has not fully adjusted to the 6.8 Ma increase in uplift rate, and that the slip gradient along the Saddle Mountains fault was established recently ( $\leq 6.8 \text{ Ma}$ ). A young establishment of this slip gradient is not mutually exclusive with the onset of clockwise rotation in the Pacific Northwest by ca. 16 Ma, and it is only indicative of how the observed clockwise rotation is resolved along individual faults and folds in the Yakima fold province.

The deformation gradient we interpret from stratigraphic and structural data likely continues, with shortening increasing to the west of transect A-A' and decreasing to the east of transect B-B'. Based on the series of fold axes orthogonal to the main trend of the Saddle Mountains anticline (Fig. 8) and mapped and inferred NW-SE-trending lateral faults (Fig. 2; Reidel, 1988), we posit that the fault-normal slip gradient is, at least partially, accommodated by a series of lateral structures, rather than simply oblique slip along the main Saddle Mountains fault plane. Broadly, paleomagnetic measurements along the Saddle Mountains show between  $10^\circ$  and  $15^\circ$  of clockwise rotation in the hanging wall of the Saddle Mountains fault since the mid-Miocene, in comparison to only  $\sim 5^\circ$  in the footwall (Fig. DR4 [see footnote 1]; Reidel et al., 1984). The exception to this is a localized area of increased clockwise rotation along the Saddle Gap segment of the Saddle Mountains anticline (Reidel et al., 1984). We attribute the localized increase of clockwise rotation to a southward bend in the Saddle Mountains anticline (Fig. DR4 [see footnote 1]). Together, the slip gradient observed in structural data and paleomagnetic data sets suggest clockwise rotation has been accommodated along the Saddle Mountains fault since Miocene time.

#### Late Pleistocene to Modern Deformation

Several lines of evidence indicate that deformation along the Saddle Mountains continues today. Using U-series analysis, we dated the youngest deformed units exposed: Ages from a steeply tilted petrocalcic horizon indicate that deformation certainly persisted until at latest 400–200 ka, and faulted petrocalcic horizons are perhaps as young as 153 ka (Figs. 6B and 11). Furthermore, modern seismicity in the Yakima fold province clusters along the Saddle Mountains fault, and epicenters are distributed along the entire length of the anticline, from the eastern Saddle Mountains to the western Boyleston Mountains, and even into Kittitas Valley (Fig. 1). Unfortunately, we cannot de-

termine a rate of deformation along the Saddle Mountains anticline from the dated petrocalcic horizons nor from the geodetic data (McCaffrey et al., 2016). While the modern rate of deformation along the Saddle Mountains cannot be determined from the currently available data, we can evaluate the long-term deformation rates along the Saddle Mountains anticline in relation to the modern, geodetically measured deformation across the entire Yakima fold province. A central assumption in our comparison is that the regional geodetic shortening rate has been sustained over the past 6.8 m.y., which is an untested hypothesis and is discussed further below.

When compared to the geodetic rate of deformation, we found that the average shortening rate accommodated across the Saddle Mountains anticline since 6.8 Ma ( $0.12\text{--}0.18 \text{ mm yr}^{-1}$ ) is between 7% and 11% of the geodetic rate of regional N-S shortening measured between longitudes  $120.1^\circ\text{W}$  and  $119.1^\circ\text{W}$  ( $\sim 1.67 \text{ mm yr}^{-1}$ ; McCaffrey et al., 2016). If we assume that the deformation rate along the Saddle Mountains anticline has remained constant since 6.8 Ma, then the vast majority of the shortening measured in the Yakima fold province must be taken up along other structures either to the north or south of the Saddle Mountains. However, several lines of evidence may suggest that the rate of deformation currently accommodated along the Saddle Mountains anticline is greater than the long-term trend determined from Miocene strata.

Paleoseismic work along the Saddle Mountains suggests that the late Quaternary to modern rate of slip along the Saddle Mountains fault is between  $0.33$  and  $0.65 \text{ mm yr}^{-1}$  (West et al., 1996), i.e.,  $\sim 2\text{--}3$  times greater than our calculated rate since 6.8 Ma, and, accordingly,  $\sim 24\text{--}30\%$  of the geodetic rate (McCaffrey et al., 2016). Additionally, there are only a handful of other Yakima folds that likely accommodate N-S shortening between  $120.1^\circ\text{W}$  and  $119.1^\circ\text{W}$ , including the Frenchman Hills anticline, the Rattlesnake Hills anticline, and the Gable Mountains, which are the eastward extension of the Umtanum anticline. GPS measurements are unable to detect shortening across any of these, or other, individual structures. Therefore, it is unlikely that any one structure accommodates the majority of the modern shortening. Last, the Saddle Mountains are topographically more prominent than these other folds and display much more seismic activity (Fig. 1). Together, these data indicate that the Saddle Mountains anticline continues to be an important tectonic structure that accommodates a component of the active N-S shortening and that the rate of deformation accommodated along the Saddle Mountains has continued to increase over geologic time.

## Implications for Seismic Hazard in Central Washington

Our estimates of the geometry and slip rate for the Saddle Mountains fault allow us to place some constraints on the seismic hazard posed by the Saddle Mountains fault by quantifying the time required to accumulate enough strain energy to produce moderate to large earthquakes along the Saddle Mountains fault. This time interval may be broadly interpreted as a proxy for recurrence intervals for earthquakes of some magnitude, given a few assumptions, as discussed next. We calculated the strain accumulation time  $t$  as  $t = M_o \sin \delta / (\mu L z \dot{s})$ , where  $M_o$  = seismic moment,  $\delta$  = dip,  $\mu$  = shear modulus,  $L$  = fault length,  $z$  = seismogenic thickness, and  $\dot{s}$  = fault slip rate. We converted  $M_o$  to moment magnitude  $M$  with the relation  $M = 2/3 \log_{10}(M_o) - 6$  (Aki and Richards, 2002). From our cross section, geologic mapping, and the modern seismicity near the Saddle Mountains, we estimated the Saddle Mountains fault dip  $\delta$  at  $37^\circ$ , the fault length  $L$  as  $\sim 116 \text{ km}$ , and earthquake rupture at depths  $z$  down to  $18 \text{ km}$ . In our calculations, we used two different slip rates: one from the

new geologic data presented in this work, and another from paleoseismic work (West et al., 1996). We provide both estimates because of the possible uncertainties associated with each fault slip rate estimate. For instance, we suggest in the preceding discussion that the rate of deformation along the Saddle Mountains anticline has increased since 6.8 Ma, and so the slip rate derived from the geologic data may be a lower bound on the modern slip rate. The higher slip rate derived from paleoseismic data may be uncertain if the paleoseismic record underestimates or overestimates the number and/or magnitude of earthquakes accommodated along the Saddle Mountains fault (McCalpin and Nelson, 1996). The calculated curves displayed in Figure 17 show the time required to accumulate sufficient strain along the Saddle Mountains fault to cause earthquakes of a given magnitude, with associated uncertainty resulting from slip rate uncertainties. We note that these curves are not frequency-magnitude distributions, but instead they represent the time between an earthquake and the next of the specified magnitude.

Interpretation of these results as proxies for recurrence interval rests on several important

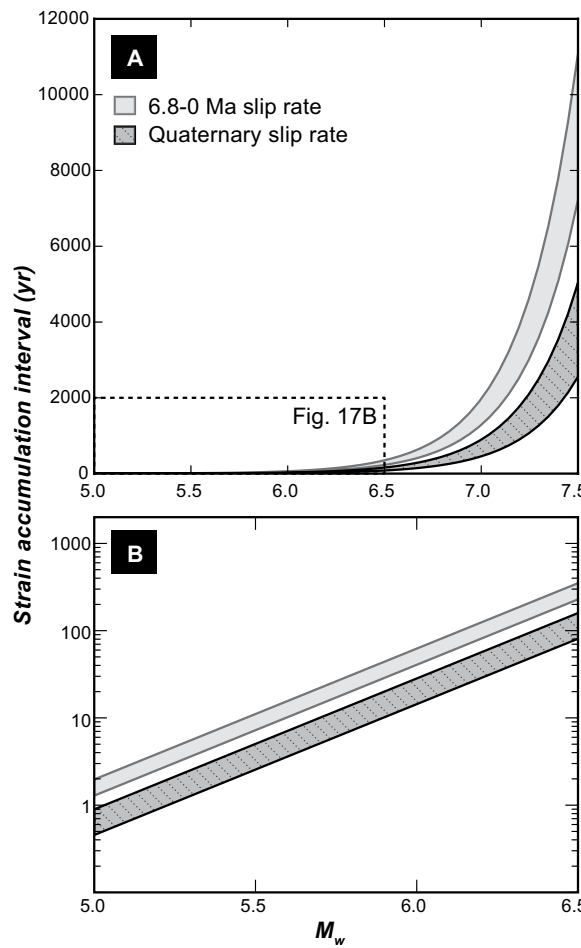


**Figure 17.** Estimates of the time required to accumulate sufficient strain energy along the Saddle Mountains fault for earthquakes of a given magnitude. (A) Linear plot of the strain accumulation interval in light gray was calculated from the paleoseismically derived slip rate estimate (West et al., 1996), and the interval in patterned dark gray was calculated from our geologically derived latest Miocene to present slip rate. (B) A log-linear plot of the same results as A to emphasize the short time interval required to accumulate strain energy for  $M = 5\text{--}6.5$  earthquakes.

assumptions. The first major assumption is that the strain accumulated on the entirety of the Saddle Mountains fault is seismically released during an earthquake. Any aseismic strain release would linearly change the results on Figure 17. For example, if 50% of the elastic strain was released aseismically, then the calculated earthquake recurrence rate would be twice that of the values shown in Figure 17. Aseismic creep has not been identified on the Saddle Mountains fault, or any of the Yakima folds, therefore suggesting that aseismic strain is minor, if present at all. The second major assumption is that each earthquake will release all of the accumulated elastic strain, so that the time until the next earthquake determines the second earthquake's magnitude. However, we know that lower-magnitude earthquakes occur along the Saddle Mountains fault (Fig. 1), so the recurrence intervals of high-magnitude earthquakes along the Saddle Mountains fault are likely longer than the values in Figure 17. That said, historic earthquakes near and on the Saddle Mountains fault are generally  $M < 3$  (Fig. 1) and rupture only a small area. Thus, the amount of energy released by smaller earthquakes is minor compared to the accumulated strain along the Saddle Mountains fault. Given these assumptions and their implications, we interpret our calculated seismicity curves to represent a slight underestimate of the time required to generate a large-magnitude earthquake, but they are generally within the correct order of magnitude.

Given the spatial extent of the Saddle Mountains fault, it is capable of generating earthquakes exceeding  $M 7$  (West et al., 1996; Casale and Pratt, 2015). If the Saddle Mountains fault only produced  $M 5\text{--}6.5$  earthquakes, we calculate that these would rupture on centennial to even annual time scales and be expected to have occurred historically (Fig. 17B). However, because  $M 5\text{--}6.5$  earthquakes have not been observed historically, we suggest that the Saddle Mountains fault is accumulating strain to be released during a larger event. Large-magnitude ruptures are found in the paleoseismic record, which shows that the most recent earthquake along the Saddle Mountains fault produced up to 6.5 m of vertical offset (West et al., 1996).

Based on the slip rate we established from 6.8 to 0 Ma, we estimated that a  $M 7$  earthquake would rupture every 1.6–2.0 k.y., or that a  $M 7.5$  earthquake would rupture every 7–11 k.y. (Fig. 17A). With the paleoseismically established slip rate from West et al. (1996), we calculated that a  $M 7$  earthquake would rupture every 0.5–1.0 k.y., or that a  $M 7.5$  earthquake would rupture every 2.5–5.0 k.y. (Fig. 17A). Overall, we find that large-magnitude earthquakes could rupture along the Saddle Moun-

tains fault every 2–11 k.y. The paleoseismic record, on the other hand, suggests that large-magnitude earthquakes have not ruptured along the Saddle Mountains fault since at least 20 k.y. (West et al., 1996). This may indicate that the paleoseismic catalog is incomplete, which is a strong possibility, given that large-magnitude earthquakes do not always rupture the surface and that the trenches excavated along the Saddle Mountains fault were not on the actual fault trace, but rather on an ancillary structure in the hanging wall (West et al., 1996).

Given the seismic hazard implications from this work, the concentration of seismic activity along the Saddle Mountains anticline, its topographic prominence, and the accelerating deformation rate, we suggest that the Saddle Mountains pose a seismic hazard to surrounding communities and infrastructure. Should a large-magnitude earthquake rupture the Saddle Mountains fault, several population centers, including Ellensburg, Yakima, and the Tri-Cities area (Richland, Pasco, and Kennewick), as well as nearby infrastructure (most importantly the Hanford Site and several large hydroelectric dams on the Columbia River) would experience strong ground shaking (Fig. 1). Last, geodetic data suggest that the Saddle Mountains accommodate only some of the measured shortening, and that other fault-cored anticlines in the Yakima fold province accommodate the remaining 70%–90% of strain energy and may be similarly capable of producing large-magnitude earthquakes.

## CONCLUSIONS

Our stratigraphic, structural, and geochronologic work in central Washington documents the history of deformation and drainage reorganization along the Saddle Mountains anticline and places important constraints on regional seismic hazards. From detailed structural and geophysical models along the Saddle Mountains, we find that shortening accommodated within the Columbia River Basalt Group has occurred since 10 Ma and that there is a westward-increasing slip gradient along the Saddle Mountains fault. This is consistent with large-scale clockwise rotation of the U.S. Pacific Northwest and suggests that vertical-axis rotation is accommodated along individual faults. We find that the fluvial strata within the Ringold Formation were sourced from central Idaho since the late Miocene, from a similar source terrane as the modern-Pleistocene Snake River. Based on our stratigraphic and structural analysis of the growth strata preserved within the Ringold Formation, we documented a previously unrecognized increase in the rate of shortening and slip accommodated along the Saddle Mountains

fault. We estimate that the average slip rate since 6.8 Ma ranges from  $0.15 \text{ mm yr}^{-1}$  in the east to  $0.23 \text{ mm yr}^{-1}$  in the west. If this slip rate has been constant since 6.8 Ma, we calculate that the time required to accumulate enough strain energy for a large-magnitude earthquake ( $M \geq 7$ ) along the Saddle Mountains fault is between 2 and 11 k.y. We note that our N-S shortening estimate is only 7%–10% of the measured geodetic shortening across northern Oregon and central Washington, suggesting that earthquake hazards posed by the Saddle Mountains faults constitute only a fraction of the total regional hazard.

## APPENDIX

### U-Pb Zircon Geochronology Methods

To analyze samples for tephra and detrital zircon age dating, zircons were separated from crushed samples using standard heavy-mineral separation techniques including a disk mill, GEMENI® table, Frantz™ isodynamic magnetic separator, and heavy liquids (methylene iodide). For tephra samples, zircon grains were handpicked under a binocular microscope. For detrital zircon samples, representative splits were obtained with a microsplitter. Zircons were mounted on slides with double-sided tape and analyzed without polishing in order to obtain ages from the outermost portion of the crystal in case of zoning.

All samples (15SM002, 15SM003, 15SM004, 15SM006, 15SM007, 15SM013, and 16SM001) were analyzed at the University of Kansas Department of Geology using a Thermo Scientific Element 2 ICP-MS attached to a Photon Machines Analyte G2 193 nm ArF excimer laser-ablation system. Laser ablation of  $20 \mu\text{m}$  circular spots was obtained at  $2.0 \text{ J cm}^{-2}$  fluency and a 10 Hz repetition rate, resulting in  $\sim 15\text{-}\mu\text{m}$ -deep pits. The ablated material was carried to the ICP in He gas with a flow rate of  $1.1 \text{ L/min}$  and tied in with Ar gas, also with a flow rate of  $1.1 \text{ L/min}$ ,  $\sim 25 \text{ cm}$  before entry into the plasma torch. Two to three natural zircon reference material standards were used for calibration and accuracy checks (GJ1 for calibration, Plešovice or Fish Canyon tuff). Elemental fractionation, downhole fractionation, and calibration drift were corrected by bracketing measurements of unknowns with the GJ1 reference material (Jackson et al., 2004) and data reduction using the VizualAge data reduction scheme (Petrus and Kamber, 2012) in the IOLITE software package (Paton et al., 2011). Two-sigma uncertainty for single spots on the GJ1 zircon standard typically range between 0.8% and 2.2% of the U-Pb age and were propagated into the uncertainty of unknowns (Table DR1 [see footnote 1]). The zircon Plešovice reference material (Sláma et al., 2008) yielded a weighted mean  $^{206}\text{Pb}/^{238}\text{U}$  date within 2% of the  $337.13 \pm 0.37$  Ma age determined by chemical abrasion-thermal ionization mass spectrometry (CA-TIMS; Sláma et al., 2008; Table DR1 [see footnote 1]). The zircon Fish Canyon tuff reference material (Schmitz and Bowring, 2001) yielded a weighted mean  $^{206}\text{Pb}/^{238}\text{U}$  date within 0.8% of the  $28.476 \pm 0.029$  Ma age determined by isotope dilution (ID)-TIMS for most U-Pb analytical sessions (Schmitz and Bowring, 2001; Table DR1 [see footnote 1]). However, for the analytical session of sample 16SM001, the Fish Canyon tuff reference zircon yielded an age of  $27.74 \pm 0.21$  Ma, which does not overlap with the uncertainty of the published ID-TIMS age (Schmitz

and Bowring, 2001; Table DR1 [see footnote 1]), but is just outside of a 2% reproducibility envelope. Therefore, the measured zircon U-Pb dates for sample 16SM001 are considered precise, but they may not be as accurate as the other age determination. This possibly renders the resulting age ~2%–3% younger than the true age of volcanic eruption. We therefore consider the measured U-Pb zircon age for 16SM001 to be a minimum.

We used the  $^{207}\text{Pb}/^{206}\text{Pb}$  date to estimate the geological age of a grain for  $^{206}\text{Pb}/^{238}\text{U}$  dates older than 1000 Ma. Single spot analyses older than 1000 Ma were considered concordant and used in age determinations if the calculated percent discordance obtained was lower than  $\pm 5\%$ . For analyses with  $^{206}\text{Pb}/^{238}\text{U}$  dates younger than 1000 Ma, an uncertainty weighted discordance (UWD) was calculated as the difference between the  $^{207}\text{Pb}/^{235}\text{U}$  and the  $^{206}\text{Pb}/^{238}\text{U}$  dates divided by the uncertainty on the  $^{207}\text{Pb}/^{235}\text{U}$  date. All analyses with UWD higher than  $\pm 1.2$  were interpreted as discordant. Data thus determined as discordant, data with large analytical errors ( $^{207}\text{Pb}/^{235}\text{U}$  age uncertainty  $>5$  Ma), and/or analyses with durations shorter than 8 s were omitted from tephra age calculations to focus the age calculations on the most accurate and reliable analytical data. Concordia plots and concordia ages for all data were derived using the ISOPLOT software (Ludwig, 2003).

### U-Series Geochronology Methods

Pedogenic material typically includes detrital clays, silts, or sand that contain  $^{232}\text{Th}$ , and some  $^{230}\text{Th}$ , that is not related to in situ  $^{234}\text{U}$  decay. Therefore, components containing detrital  $^{230}\text{Th}$  must be identified and removed as much as possible prior to analysis, or accounted for using  $^{232}\text{Th}$  as a monitor of detrital contamination. Calcified roots were mechanically cleaned using carbide rotary dental burs to remove visible detritus adhering to the exterior of rhizoliths (Fig. 11A). Calcic rinds or stringers within the cemented matrix were sampled using 1-mm-diameter dental burs to remove soft or detrital-rich material for the same purpose of reducing  $^{230}\text{Th}$  from detrital sources (Figs. 11B and 11C). Once cleaned, subsamples from multiple roots and pedogenic rinds from each unit were obtained by milling with a small dental drill, and the resulting powder was collected for isotopic analyses. Ideally, results for aliquots from the same unit will have similar ages, increasing confidence that calcification represents a single pedogenic event.

Rhizoliths and rind aliquots were weighed and spiked with a high-purity mixed isotope tracer that contained a known amount of isotopes  $^{236}\text{U}$ - $^{235}\text{U}$ - $^{229}\text{Th}$ . Samples were digested at 1 atm and temperatures between 105 °C and 125 °C with nitric and hydrochloric acid in Teflon™ perfluoroalkoxy (PFA) copolymer resin vials. The carbonate components were dissolved in this step, but any authigenic opal or detrital silicate material remained undissolved. To avoid laboratory fractionation of U and Th and erroneous  $^{230}\text{Th}/\text{U}$  ages, any remaining residue was separated and digested in hydrofluoric acid and then recombined with the original solute. The resulting analyses thus represent total digestion, and  $^{230}\text{Th}/^{238}\text{U}$  measurements accurately represent values inherent in the subsamples. U and Th were purified using standard ion chromatographic methods with Biorad™ AG1x8 (200–400 mesh) resin. The separated U salts were loaded on rhenium double-filament assemblies, whereas Th salts were loaded on single rhenium filaments sandwiched between layers of graphite suspension. Isotopic ratios were obtained on a Thermo Finnigan Triton™ TIMS equipped with

a retarding potential quadrupole electrostatic (RPQ) filter and a single ETP™ discrete-dynode electron multiplier operating in peak-jumping mode. Measured  $^{234}\text{U}/^{235}\text{U}$ ,  $^{236}\text{U}/^{235}\text{U}$ ,  $^{230}\text{Th}/^{229}\text{Th}$ , and  $^{232}\text{Th}/^{229}\text{Th}$  ratios were corrected for mass fractionation, spike contribution, and procedural blank addition, and they were normalized relative to a  $^{234}\text{U}/^{238}\text{U}$  atomic ratio value of 0.0000529 obtained from National Institute of Standards and Technology (NIST) U-standard SRM4321 measured along with samples. Reported values for  $^{234}\text{U}/^{238}\text{U}$  AR were derived from measured  $^{234}\text{U}/^{235}\text{U}$  atom ratios assuming a  $^{234}\text{U}/^{238}\text{U}$  atom ratio of 137.88 (Steiger and Jäger, 1977).

The  $^{230}\text{Th}/\text{U}$  ages and initial isotopic ratios for individual subsamples were calculated after mathematically removing contributions from a detrital component (Ludwig and Titterington, 1994; Ludwig and Paces, 2002). Detritus-corrected  $^{230}\text{Th}/^{238}\text{U}$  and  $^{234}\text{U}/^{238}\text{U}$  AR values were obtained using measured  $^{232}\text{Th}/^{238}\text{U}$  AR values and the assumptions that the detritus had a uniform U/Th composition similar to average continental crust (Shaw et al., 1976; Taylor and McLennan, 1985; Rudnick and Gao, 2003) and was in radioactive secular equilibrium (that is, a composition of  $^{230}\text{Th}/^{238}\text{U}$  AR =  $1.276 \pm 0.64$ ;  $^{230}\text{Th}/^{238}\text{U}$  AR =  $1.0 \pm 0.25$ ;  $^{234}\text{U}/^{238}\text{U}$  AR =  $1.0 \pm 0.1$ ). Uncertainties were propagated through the age calculation such that errors are only slightly larger than those derived solely from analytical uncertainties if measured  $^{232}\text{Th}/^{238}\text{U}$  AR is negligible (say  $<<0.1$ ), but they may be much larger if substantial amounts of  $^{232}\text{Th}$  were present (i.e.,  $^{232}\text{Th}/^{238}\text{U}$  AR  $>0.2$ ). Ages and initial ratios were calculated using routines in the program Isoplot/Ex (Ludwig, 2012) and decay constants for  $^{234}\text{U}$  and  $^{230}\text{Th}$  from Cheng et al. (2013). Measured AR values, detritus-corrected AR values, and finite ages given by the first-derivative age solutions are reported in Table DR10 (see footnote 1). Uncertainties are reported at the  $2\sigma$  level and include errors associated with analytical counting statistics, reproducibility from analyses of standards, and uncertainty propagated from any detrital component present. Additional information on standard operating procedure USGS-DRIL-01, R0 Uranium-Thorium Disequilibrium Studies for U-series age analysis, is available on request.

Several standards of known age, including a sample of 69.3 Ma uranium ore in U-series secular equilibrium (Ludwig et al., 1985) and a  $119.6 \pm 1.9$  ka coral dating standard (Watanabe and Nakai, 2006), were run along with unknown samples to ensure data quality. Measured and known standard isotopic ratios are available in Table DR11 (see footnote 1).

### ACKNOWLEDGMENTS

This work was supported by the U.S. Geological Survey Mendenhall Fellowship awarded to Staisch. We thank Ray Wells and Gabriele Casale for their thoughtful reviews. We also thank Ethan Hyland, Scott Bennett, John Lasher, and Barbara Brim for their assistance in the field. We appreciate the access granted to us by landowners, especially Gary and Nathan Maughan for road access. Any use of trade, firm, or product names is for descriptive purposes only and does not imply endorsement by the U.S. government.

### REFERENCES CITED

- Aki, K., and Richards, P.G., 2002, Quantitative Seismology, Volume 1: Sausalito, California, University Science Books, 700 p.
- Allmendinger, R.W., 1998, Inverse and forward numerical modeling of trishear fault-propagation folds: Tectonics, v. 17, p. 640–656, doi:10.1029/98TC01907.
- Allmendinger, R.W., and Shaw, J.H., 2000, Estimation of fault propagation distance from fold shape: Implications for earthquake hazard assessment: Geology, v. 28, p. 1099–1102, doi:10.1130/0091-7613(2000)28<1099:EOFPDF>2.0.CO;2.
- Barry, T.L., Kelley, S.P., Reidel, S.P., Camp, V.E., Self, S., Jarboe, N.A., Duncan, R.A., and Renne, P.R., 2013, Eruption chronology of the Columbia River Basalt Group, in Reidel, S.P., Camp, V.E., Ross, M.E., Wolff, J.A., Martin B.S., Tolan, T.L., and Wells, R.E., eds., The Columbia River Flood Basalt Province: Geological Society of America Special Paper 497, p. 45–66, doi:10.1130/2013.2497(02).
- Benjamin and Associates, URS Corporation, Geomatics Consultants, and Shannon & Wilson, 2012, Probabilistic Seismic Hazard Analyses Project for the Mid-Columbia Dams: Prepared for Public Utilities Districts of Chelan, Douglas, and Grant Counties, Washington, Benjamin and Associates, 344 p.
- Bentley, R.D., 1977, Stratigraphy of the Yakima basalts and structural evolution of the Yakima ridges in the western Columbia Plateau, in Brown, E.H., and Ellis, R.C., eds., Geology Excursions in the Pacific Northwest: Bellingham, Washington, Western Washington University Press, p. 339–389.
- Beranek, L.P., Link, P.K., and Fanning, C.M., 2006, Miocene to Holocene landscape evolution of the western Snake River Plain region, Idaho: Using the SHRIMP detrital zircon provenance record to track eastward migration of the Yellowstone hotspot: Geological Society of America Bulletin, v. 118, p. 1027–1050, doi:10.1130/B25896.1.
- Blakely, R.J., Sherrod, B.L., Weaver, C.S., Wells, R.E., Rohay, A.C., Barnett, E.A., and Knepprath, N.E., 2011, Connecting the Yakima fold and thrust belt to active faults in the Puget Lowland, Washington: Journal of Geophysical Research—Solid Earth, v. 116, B07105, doi:10.1029/2010JB008091.
- Bond, J.G., Kauffman, J.D., and Miller, D.A., and Venkatakrishnan, Ramesh, 1978, Geologic Map of Idaho: Moscow, Idaho, Idaho Bureau of Mines and Geology, with contributions from U.S. Geological Survey, scale 1:500,000.
- Camp, V.E., 1981, Geologic studies of the Columbia Plateau: Part II. Upper Miocene basalt distribution, reflecting source locations, tectonism, and drainage history in the Clearwater embayment, Idaho: Geological Society of America Bulletin, v. 92, p. 669–678, doi:10.1130/0016-7606(1981)92<669:GSOTCP>2.0.CO;2.
- Campbell, N.P., and Bentley, R.D., 1981, Late Quaternary deformation of the Toppenish Ridge uplift in south-central Washington: Geology, v. 9, p. 519–524, doi:10.1130/0091-7613(1981)9<519:LQDOTT>2.0.CO;2.
- Carroll, A.R., and Bohacs, K.M., 1999, Stratigraphic classification of ancient lakes: Balancing tectonic and climatic controls: Geology, v. 27, p. 99–102, doi:10.1130/0091-7613(1999)027<0099:SCOALB>2.3.CO;2.
- Casale, G., and Pratt, T.L., 2015, Thin- or thick-skinned faulting in the Yakima fold and thrust belt (WA)? Constraints from kinematic modeling of the Saddle Mountains anticline: Bulletin of the Seismological Society of America, v. 105, p. 745–752, doi:10.1785/0120140050.
- Cheney, E.S., 2014, Tertiary stratigraphy and structure of the eastern flank of the Cascade Range, Washington, in Dashtgard, S., and Ward, B., eds., Trials and Tribulations of Life on an Active Subduction Zone: Field Trips in and around Vancouver, Canada: Geological Society of America Field Guide 38, p. 193–226, doi:10.1130/2014.0038(09).
- Cheng, H., Edwards, R.L., Shen, C.C., Polyak, V.J., Asmerom, Y., Woodhead, J., Hellstrom, J., Wang, Y., Kong, X., Spötl, C., and Wang, X., 2013, Improvements in  $^{230}\text{Th}$  dating,  $^{230}\text{Th}$  and  $^{234}\text{U}$  half-life values, and U-Th isotopic measurements by multicollector inductively coupled plasma mass spectrometry: Earth and Planetary Science Letters, v. 371–372, p. 82–91, doi:10.1016/j.epsl.2013.04.006.
- Choiniere, S., and Swanson, D., 1979, Magnetostratigraphy and correlation of Miocene basalts of the northern Oregon Coast and Columbia Plateau, southeast Washington: American Journal of Science, v. 279, p. 755–777, doi:10.2475/ajs.279.7.755.

- Coe, R.S., Bogue, S., and Myers, C.W., 1978, Paleomagnetism of the Grande Ronde (Lower Yakima) Basalt Exposed at Sentinel Gap: Potential Use for Stratigraphic Correlation: Rockwell Hanford Operations Report RHO-BWI-ST-2, 28 p.
- Czajkowski, J.L., Bowman, J.D., Schuster, J.E., and Wheeler, C.M., 2012 (rev. 2015), Oil and Gas Wells in Washington State: Washington Division of Geology and Earth Resources Open-File Report 2012-02, 1 Microsoft Excel file plus 4 p. text.
- Dahlstrom, C.D.A., 1969, Balanced cross sections: Canadian Journal of Earth Sciences, v. 6, p. 743–757, doi: 10.1139/e69-069.
- Dickinson, W.R., and Gehrels, G.E., 2009, Use of U-Pb ages of detrital zircons to infer maximum depositional ages of strata: A test against a Colorado Plateau Mesozoic database: Earth and Planetary Science Letters, v. 288, no. 1–2, p. 115–125, doi: 10.1016/j.epsl.2009.09.013.
- Fiske, R.S., 1963, Subaqueous pyroclastic flows of the Ohanapeosh Formation, Washington: Geological Society of America Bulletin, v. 74, p. 391–406, doi: 10.1130/0016-7606(1963)74[391:SPFITO]2.0.CO;2.
- Gehrels, G.E., 2000, Introduction to detrital zircon studies of Paleozoic and Triassic strata in western Nevada and northern California, in Soreghan, M.J., and Gehrels, G.E., eds., Paleozoic and Triassic Paleogeography and Tectonics of Western Nevada and Northern California: Geological Society of America Special Paper 347, p. 1–17, doi: 10.1130/0-8137-2347-7.1.
- Geomatix Consultants, 1996, Probabilistic Seismic Hazard Analysis DOE Hanford Site, Washington: Geomatix Consultants Report WHC-SD-W236A-TI-002, Rev. 1, 372 p., <http://pdw.hanford.gov/arpir/pdf.cfm?accession=D196005995>.
- Geslin, J.K., Link, P.K., and Fanning, C.M., 1999, High-precision provenance determination using detrital-zircon ages and petrography of Quaternary sands on the eastern Snake River Plain, Idaho: Geology, v. 27, p. 295–298, doi: 10.1130/0091-7613(1999)027<0295:HPPDUD>2.3.CO;2.
- Geslin, J.K., Link, P.K., Riesterer, J.W., Kuntz, M.A., and Fanning, C.M., 2002, Pliocene and Quaternary stratigraphic architecture and drainage systems of the Big Lost Trough, northeastern Snake River Plain, Idaho, in Link, P.K., and Mink, L.L., eds., Geology, Hydrogeology, and Environmental Remediation: Idaho National Engineering and Environmental Laboratory, Eastern Snake River Plain, Idaho: Geological Society of America Special Paper 353, p. 11–26, doi: 10.1130/0-8137-2353-1.11.
- Gilmour, L.A., 2012, U/Pb Ages of Eocene and Younger Rocks on the Eastern Flank of the Central Cascade Range, Washington, USA [M.S. thesis]: Seattle, Washington, University of Washington, 50 p.
- Gradstein, F.M., Ogg, J.G., Hilgen, F.J., 2012, Geomagnetic polarity time scale, in Gradstein, F.M., Ogg, J.G., Schmitz, M., and Ogg, G., eds., The Geologic Time Scale 2012 2-Volume Set: Elsevier B.V., p. 85–113, doi: 10.1016/B978-0-444-59425-9.00005-6.
- Hooper, P.R., Knowles, C.R., and Watkins, N.D., 1979, Magnetostratigraphy of the Imnaha and Grande Ronde Basalts in the southeastern part of the Columbia Plateau: American Journal of Science, v. 279, p. 737–754, doi: 10.2475/aj.s.279.7.737.
- Jackson, S.E., Pearson, N.J., Griffin, W.L., and Belousova, E.A., 2004, The application of laser ablation-inductively coupled plasma-mass spectrometry to in situ U-Pb zircon geochronology: Chemical Geology, v. 211, p. 47–69, doi: 10.1016/j.chemgeo.2004.06.017.
- Janecke, S.U., VanDenburg, C.J., Blankenau, J.J., and M'Gonigle, J.W., 2000, Long-distance longitudinal transport of gravel across the Cordilleran thrust belt of Montana and Idaho: Geology, v. 28, p. 439–442, doi: 10.1130/0091-7613(2000)28<439:LLTOGA>2.0.CO;2.
- Johnson, B.R., and Raines, G.L., 1995, Digital Map of Major Bedrock Lithologic Units for the Pacific Northwest: A Contribution to the Interior Columbia Basin Ecosystem Management Project: U.S. Geological Survey Open-File Report 95-680.
- Jutzeler, M., McPhie, J., and Allen, S.R., 2014, Facies architecture of a continental, below-wave-base volcanoclastic basin: The Ohanapeosh Formation, ancestral Cascades arc (Washington, USA): Geological Society of America Bulletin, v. 126, p. 352–376, doi: 10.1130/B30763.1.
- Keller, E.A., Gurrula, L., and Tierney, T.E., 1999, Geomorphic criteria to determine direction of lateral propagation of reverse faulting and folding: Geology, v. 27, p. 515–518, doi: 10.1130/0091-7613(1999)027<0515:GCTDDO>2.3.CO;2.
- Lamb, A., Blakely, R.J., Sherrod, B.L., Wells, R.E., and Brocher, T.M., 2015, Investigating relationships between the Yakima fold and thrust belt and basement structure in Washington State using matched filtering of gravity and high-resolution aeromagnetic data, in American Geophysical Union–Society of Exploration Geophysicists Workshop: Keystone, Colorado, American Geophysical Union.
- Lindsey, K.A., 1996, The Miocene to Pliocene Ringold Formation and Associated Deposits of the Ancestral Columbia River System, South-Central Washington and North-Central Oregon: Washington Division of Geology and Earth Resources Open-File Report 96-8, 176 p.
- Lindsey, K.A., and Gaylord, D.R., 1990, Lithofacies and sedimentology of the Miocene–Pliocene Ringold Formation, Hanford Site, south-central Washington: Northwest Science, v. 64, p. 165–180.
- Link, P.K., Fanning, C.M., and Beranek, L.P., 2005, Reliability and longitudinal change of detrital-zircon age spectra in the Snake River system, Idaho and Wyoming: An example of reproducing the bumpy barcode: Sedimentary Geology, v. 182, p. 101–142, doi: 10.1016/j.sedgeo.2005.07.012.
- Ludwig, K.R., 2003, User's Manual for Isoplot 3.00: A Geochronological Toolkit for Microsoft Excel: Berkeley Geochronology Center Special Publication 4, 74 p.
- Ludwig, K.R., 2012, Isoplot 3.75: A Geochronology Toolkit for Microsoft Excel: Berkeley Geochronology Center Special Publication 5, 75 p.
- Ludwig, K.R., and Paces, J.B., 2002, Uranium-series dating of pedogenic silica and carbonate, Crater Flat, Nevada: Geochimica et Cosmochimica Acta, v. 66, p. 487–506, doi: 10.1016/S0016-7037(01)00786-4.
- Ludwig, K.R., and Titterington, D.M., 1994, Calculation of <sup>230</sup>Th/U isochrons, ages, and errors: Geochimica et Cosmochimica Acta, v. 58, no. 22, p. 5031–5042, doi: 10.1016/0016-7037(94)90229-1.
- Ludwig, K.R., Wallace, A.R., and Simmons, K.R., 1985, The Schwartzwalder uranium deposit: II. Age of uranium mineralization and lead isotope constraints on genesis: Economic Geology and the Bulletin of the Society of Economic Geologists, v. 80, p. 1858–1871, doi: 10.2113/gsecongeo.80.7.1858.
- Malone, S.D., Roth, G.H., and Smith, S.W., 1975, Details of microseismic earthquake swarms in the Columbia Basin, Washington: Bulletin of the Seismological Society of America, v. 65, p. 855–864.
- McCaffrey, R., Long, M.D., Goldfinger, C., Zwick, P.C., Nabelek, J.L., Johnson, C.K., and Smith, C., 2000, Rotation and plate locking at the southern Cascadia subduction zone: Geophysical Research Letters, v. 27, p. 3117–3120, doi: 10.1029/2000GL011768.
- McCaffrey, R., Qamar, A.I., King, R.W., Wells, R., Khazadze, G., Williams, C.A., Stevens, C.W., Vollick, J.J., and Zwick, P.C., 2007, Fault locking, block rotation and crustal deformation in the Pacific Northwest: Geophysical Journal International, v. 169, p. 1315–1340, doi: 10.1111/j.1365-246X.2007.03371.x.
- McCaffrey, R., King, R.W., Payne, S.J., and Lancaster, M., 2013, Active tectonics of northwestern U.S. inferred from GPS-derived surface velocities: Journal of Geophysical Research—Solid Earth, v. 118, p. 709–723, doi: 10.1029/2012JB009473.
- McCaffrey, R., King, R.W., Wells, R.E., Lancaster, M., and Miller, M.M., 2016, Contemporary deformation in the Yakima fold and thrust belt estimated with GPS: Geophysical Journal International, v. 207, p. 1–11, doi: 10.1093/gji/ggw252.
- McCalpin, J.P., and Nelson, A.R., 1996, Introduction to paleoseismology, in McCalpin, J.A., ed., Paleoseismology: New York, Academic Press, International Geophysics Series, Volume 95, p. 1–32, doi: 10.1016/S0074-6142(96)80068-4.
- Miller, B.A., 2014, On the Origin of Umtanum Ridge: Kinematics of Neogene Slip [M.S. thesis]: Seattle, Washington, University of Washington, 47 p.
- Miller, R.B., Gordon, S.M., Bowring, S.A., Doran, B.A., McLean, N.M., Michels, Z.D., Shea, E.K., Whitney, D.L., Wintzer, N.E., and Mendoza, M.K., 2009, Linking deep and shallow crustal processes in an exhumed continental arc, North Cascades, Washington, in O'Connor, J.E., Dorsey, R.J., and Madin, I.P., eds., Volcanoes to Vineyards: Geologic Field Trips through the Dynamic Landscape of the Pacific Northwest: Geological Society of America Field Guide 15, p. 373–406, doi: 10.1130/2009.fl015(19).
- Mitra, S., 1990, Fault-propagation folds: Geometry, kinematic evolution, and hydrocarbon traps: American Association of Petroleum Geologists Bulletin, v. 74, p. 921–945.
- Morgan, J.K., and Morgan, N.H., 1995, A new species of *Capromeryx* (Mammalia: Artiodactyla) from the Taunton local fauna of Washington, and the correlation with other Blancan faunas of Washington and Idaho: Journal of Vertebrate Paleontology, v. 15, p. 160–170, doi: 10.1080/02724634.1995.10011215.
- Olsen, P.E., 1990, Tectonic, climatic, and biotic modulation of lacustrine ecosystems—Examples from Newark Supergroup of eastern North America, in Katz, B., ed., Lacustrine Basin Exploration: Case Studies and Modern Analogs: American Association of Petroleum Geologists Memoir 50, p. 209–224.
- Packer, D.R., and Johnson, J.M., 1979, Paleomagnetism and age dating of the Ringold Formation and loess deposits in the State of Washington: Oregon Geology, v. 41, p. 119–132.
- Paton, C., Hellstrom, J., Paul, B., Woodhead, J., and Herdt, J., 2011, Iolite: Freeware for the visualisation and processing of mass spectrometric data: Journal of Analytical Atomic Spectrometry, v. 26, p. 2508–2518, doi: 10.1039/c1ja10172b.
- Petrus, J.A., and Kamber, B.S., 2012, VizualAge: A novel approach to laser ablation ICP-MS U-Pb geochronology data reduction: Geostandards and Geoanalytical Research, v. 36, p. 247–270, doi: 10.1111/j.1751-908X.2012.00158.x.
- Pratt, T.L., 2012, Large-scale splay faults on a strike-slip fault system: The Yakima Folds, Washington State: Geochemistry Geophysics Geosystems, v. 13, Q11004, doi: 10.1029/2012GC004405.
- Press, W.H., Flannery, B.P., Teukolsky, S.A., and Vetterling, W.T., 1986, Numerical recipes, in The Art of Scientific Computing: Cambridge, Cambridge University Press, 818 p.
- Reidel, S.P., 1983, Stratigraphy and petrogenesis of the Grande Ronde Basalt from the deep canyon country of Washington, Oregon, and Idaho: Geological Society of America Bulletin, v. 94, p. 519–542, doi: 10.1130/0016-7606(1983)94<519:SAPOTG>2.0.CO;2.
- Reidel, S.P., 1984, The Saddle Mountains: The evolution of an anticline in the Yakima fold belt: American Journal of Science, v. 284, p. 942–978, doi: 10.2475/ajs.284.8.942.
- Reidel, S.P., 1988, Geologic Map of the Saddle Mountains, South-Central Washington: Washington Division of Geology and Earth Resources Map GM-38, scale 1:48,000, 5 sheets.
- Reidel, S.P., and Fecht, K.R., 1981, Wanapum and Saddle Mountains Basalts of the Cold Creek Syncline Area, Surface Geology of the Cold Creek Syncline: Rockwell Hanford Operations Report RHO-BWI-ST-14, 45 p.
- Reidel, S.P., and Fecht, K.R., 1987, The Huntzinger Flow: Evidence of surface mixing of the Columbia River Basalt and its petrogenetic implications: Geological Society of America Bulletin, v. 98, p. 664–677, doi: 10.1130/0016-7606(1987)98<664:THFEOS>2.0.CO;2.
- Reidel, S.P., Scott, G.R., Bazard, D.R., Cross, R.W., and Dick, B., 1984, Post-12 million year clockwise rotation in the central Columbia Plateau, Washington: Tectonics, v. 3, p. 251–273, doi: 10.1029/TC003i002p00251.
- Reidel, S.P., Fecht, K.R., Hagood, M.C., and Tolan, T.L., 1989a, The geologic evolution of the central Columbia Plateau, in Reidel, S.P., and Hooper, P.R., eds., Volcanism and Tectonism in the Columbia River Flood-

- Basalt Province: Geological Society of America Special Paper 239, p. 247–264, doi:10.1130/SPE239-p247.
- Reidel, S.P., Tolan, T.L., Hooper, P.R., Beeson, M.H., Fecht, K.R., Bentley, R.D., and Anderson, J.L., 1989b, The Grande Ronde Basalt, Columbia River Basalt Group: Stratigraphic descriptions and correlations in Washington, Oregon, and Idaho, in Reidel, S.P., and Hooper, P.R., eds., Volcanism and Tectonism in the Columbia River Flood-Basalt Province: Geological Society of America Special Paper 239, p. 21–54, doi:10.1130/SPE239-p21.
- Reidel, S.P., Campbell, N.P., Fecht, K.R., and Lindsey, K.A., 1994, Late Cenozoic Structure and Stratigraphy of South-Central Washington, in Lasmannis, R., and Cheney, E.S., eds., Regional Geology of Washington State: Washington Division of Geology and Earth Resources Bulletin 80, p. 159–180.
- Reidel, S.P., Camp, V.E., Tolan, T.L., Kauffman, J.D., and Garwood, D.L., 2013, Tectonic evolution of the Columbia River flood basalt province, in Reidel, S.P., Camp, V.E., Ross, M.E., Wolff, J.A., Martin, B.S., Tolan, T.L., and Wells, R.E., eds., The Columbia River Flood Basalt Province: Geological Society of America Special Paper 497, p. 293–324, doi:10.1130/2013.2497(12).
- Repennin, C.A., 1987, Biochronology of the microtine rodents of the United States, in Woodburne, M.O., ed., Cenozoic Mammals of North America: Geochronology and Biostratigraphy: Berkeley, California, University of California Press, p. 236–268.
- Rowan, M.G., and Linares, R., 2000, Fold-evolution matrices and axial-surface analysis of fault bend folds: Application to the Medina anticline, Eastern Cordillera, Colombia: American Association of Petroleum Geologists Bulletin, v. 84, p. 741–764.
- Rudnick, R.L., and Gao, S., 2003, Composition of the continental crust, in Holland, H.D., and Turekian, K.K., eds., Treatise on Geochemistry: San Diego, California, Elsevier, p. 1–64, doi:10.1016/B0-08-043751-6/03016-4.
- Saltus, R.W., 1993, Upper-crustal structure beneath the Columbia River Basalt Group, Washington: Gravity interpretation controlled by borehole and seismic studies: Geological Society of America Bulletin, v. 105, p. 1247–1259, doi:10.1130/0016-7606(1993)105<1247:UCSBTC>2.3.CO;2.
- Saylor, J.E., and Sundell, K.E., 2016, Quantifying comparison of large detrital geochronology data sets: Geosphere, v. 12, p. 203–220, doi:10.1130/GES01237.1.
- Schmitz, M.D., and Bowring, S.A., 2001, U-Pb zircon and titanite systematics of the Fish Canyon Tuff: An assessment of high-precision U-Pb geochronology and its application to young volcanic rocks: *Geochimica et Cosmochimica Acta*, v. 65, p. 2571–2587, doi:10.1016/S0016-7037(01)00616-0.
- Shaw, D.M., Dostal, J., and Keays, R.R., 1976, Additional estimates of continental surface Precambrian shield composition in Canada: *Geochimica et Cosmochimica Acta*, v. 40, p. 73–83, doi:10.1016/0016-7037(76)90195-2.
- Sláma, J., Košler, J., Condon, D.J., Crowley, J.L., Gerdes, A., Hanchar, J.M., Horstwood, M.S., Morris, G.A., Nasdala, L., Norberg, N., and Schaltegger, U., 2008, Plešovice zircon—A new natural reference material for U-Pb and Hf isotopic microanalysis: *Chemical Geology*, v. 249, p. 1–35, doi:10.1016/j.chemgeo.2007.11.005.
- Smith, G.A., 1988, Neogene synvolcanic and syntectonic sedimentation in central Washington: *Geological Society of America Bulletin*, v. 100, p. 1479–1492, doi:10.1130/0016-7606(1988)100<1479:MS>2.3.CO;2.
- Smith, G.A., 1993, Missoula flood dynamics and magnitudes inferred from sedimentology of slack-water deposits on the Columbia Plateau, Washington: *Geological Society of America Bulletin*, v. 105, p. 77–100, doi:10.1130/0016-7606(1993)105<0077:MFDAM>2.3.CO;2.
- Steiger, R.H., and Jäger, E., 1977, Subcommission on Geochronology: Convention on use of decay constants in geochronology and cosmochronology: *Earth and Planetary Science Letters*, v. 36, p. 359–362, doi:10.1016/0012-821X(77)90060-7.
- Stewart, J.H., Gehrels, G.E., Barth, A.P., Link, P.K., Christie-Blick, N., and Wrucke, C.T., 2001, Detrital zircon provenance of Mesoproterozoic to Cambrian arenites in the western United States and northwestern Mexico: *Geological Society of America Bulletin*, v. 113, p. 1343–1356, doi:10.1130/0016-7606(2001)113<1343:DZPOMT>2.0.CO;2.
- Suppe, J., 1985, Principles of Structural Geology: Englewood Cliffs, New Jersey, Prentice-Hall, 537 p.
- Suppe, J., and Medwedeff, D.A., 1990, Geometry and kinematics of fault-propagation folding: *Eclogae Geologicae Helvetiae*, v. 83, p. 409–454.
- Suppe, J., Chou, G.T., and Hook, S.C., 1992, Rates of folding and faulting determined from growth strata, in McClay, K.R., ed., Thrust Tectonics: London, Chapman and Hall, p. 105–121, doi:10.1007/978-94-011-3066-0\_9.
- Swanson, D.A., Wright, T.L., Hooper, P.R., and Bentley, R.D., 1979, Revisions in Stratigraphic Nomenclature of the Columbia River Basalt Group: U.S. Geological Survey Bulletin 1457-G, 59 p.
- Tabor, R.W., Frizzell, V.A., Swanson, D.A., Byerly, G.R., and Bentley, R.D., 1982, Geologic Map of the Wenatchee 1:100,000 Quadrangle, Central Washington: U.S. Geological Survey Miscellaneous Investigations Series Map I-1311 scale 1:100,000.
- Tabor, R.W., Frizzell, V.A., Vance, J.A., and Naeser, C.W., 1984, Ages and stratigraphy of Lower and Middle Tertiary sedimentary and volcanic rocks of the central Cascades, Washington: Application to the tectonic history of the Straight Creek fault (USA): *Geological Society of America Bulletin*, v. 95, p. 26–44, doi:10.1130/0016-7606(1984)95<26:AASOLA>2.0.CO;2.
- Tabor, R.W., Frizzell, V.A., Jr., Booth, D.B., and Waitt, R.B., 2000, Geologic Map of the Snoqualmie Pass 30' × 60' Quadrangle, Washington: U.S. Geological Survey Scientific Investigations Map I-2538, scale 1:100,000.
- Taylor, S.R., and McLennan, S.M., 1985, The Continental Crust—Its Composition and Evolution: Palo Alto, California, Blackwell Scientific Publishers, 312 p.
- Tolan, T.L., Martin, B.S., Reidel, S.P., Anderson, J.L., Lindsey, K.A., and Burt, W., 2009, An introduction to the stratigraphy, structural geology, and hydrogeology of the Columbia River flood basalt province: A primer for the GSA Columbia River Basalt Group field trips, in O'Connor, J.E., Dorsey, R.J., and Madin, I.P., eds., Volcanoes to Vineyards—Geologic Field Trips through the Dynamic Landscape of the Pacific Northwest: Geological Society of America Field Guide 15, p. 599–643, doi:10.1130/2009.fl015(28).
- Watanabe, Y., and Nakai, S.I., 2006, U-Th radioactive disequilibrium analyses for JCp-1, coral reference distributed by the Geological Survey of Japan: *Geochemical Journal*, v. 40, p. 537–541, doi:10.2343/geochemj.40.537.
- Watters, T.R., 1989, Periodically spaced anticlines of the Columbia Plateau, in Reidel, S.P., and Hooper, P.R., eds., Volcanism and Tectonism in the Columbia River Flood-Basalt Province: Geological Society of America Special Paper 239, p. 283–292, doi:10.1130/SPE239-p283.
- Wells, R.E., Weaver, C.S., and Blakely, R.J., 1998, Fore-arc migration in Cascadia and its neotectonic significance: *Geology*, v. 26, p. 759–762, doi:10.1130/0091-7613(1998)026<0759:FAMICA>2.3.CO;2.
- Wells, R.E., and McCaffrey, R., 2013, Steady rotation of the Cascade arc: *Geology*, v. 41, p. 1027–1030, doi:10.1130/G34514.1.
- Wells, R.E., Simpson, R.W., Bentley, R.D., Beeson, M.H., Mangan, M.T., and Wright, T.L., 1989, Correlation of Miocene flows of the Columbia River Basalt Group from the central Columbia River Plateau to the coast of Oregon and Washington, in Reidel, S.P., and Hooper, P.R., eds., Volcanism and Tectonism in the Columbia River Flood-Basalt Province: Geological Society of America Special Paper 239, p. 113–130, doi:10.1130/SPE239-p113.
- West, M.W., Ashland, F.X., Busacca, A.J., Berger, G.W., and Shaffer, M.E., 1996, Late Quaternary deformation, Saddle Mountains anticline, south-central Washington: *Geology*, v. 24, p. 1123–1126, doi:10.1130/0091-7613(1996)024<1123:LQDSMA>2.3.CO;2.
- Wilkerson, S.M., Apotria, T., and Farid, T., 2002, Interpreting the geologic map expression of contractional fault-related fold terminations: Lateral/oblique ramps versus displacement gradients: *Journal of Structural Geology*, v. 24, p. 593–607, doi:10.1016/S0191-8141(01)00111-0.
- Wilson, M.S., Dyman, T.S., and Condon, S.M., 2008, Evaluation of well-test results and the potential for basin-central gas in the Columbia Basin, central Washington, in U.S. Geological Survey Eastern Oregon and Washington Province Assessment Team, eds., Geologic Assessment of Undiscovered Gas Resources of the Eastern Oregon and Washington Province: U.S. Geological Survey Digital Data Series 69-O, CD-ROM.

SCIENCE EDITOR: DAVID I. SCHOFIELD  
ASSOCIATE EDITOR: STEPHEN T. JOHNSTON

MANUSCRIPT RECEIVED 27 FEBRUARY 2017  
REVISED MANUSCRIPT RECEIVED 5 JULY 2017  
MANUSCRIPT ACCEPTED 16 AUGUST 2017

Printed in the USA